

The steady motion of a semi-infinite bubble through a flexible-walled channel

By DONALD P. GAVER III,¹ DAVID HALPERN,²
OLIVER E. JENSEN³ AND JAMES B. GROTBORG⁴

¹Department of Biomedical Engineering, Tulane University, New Orleans, LA 70118, USA

²Department of Mathematics, University of Alabama, Tuscaloosa, AL 35487, USA

³Department of Mathematics and Statistics, University of Newcastle upon Tyne,
Newcastle upon Tyne, NE1 7RU, UK

⁴Departments of Biomedical Engineering and Anesthesia, Northwestern University, Evanston,
IL 60208, USA

(Received 26 August 1995 and in revised form 2 January 1996)

We performed a theoretical investigation of the progression of a finger of air through a liquid-filled flexible-walled channel—an initial model of pulmonary airway reopening. Positive pressure, P_b^* , drives the bubble forward, and separates flexible walls that are modelled as membranes under tension, T , supported by linearly elastic springs with elasticity K . The gap width between the walls under stress-free conditions is $2H$, and the liquid has constant surface tension, γ , and viscosity, μ . Three parameters define the state of the system: $Ca = \mu U/\gamma$ is a dimensionless velocity that represents the ratio of viscous to capillary stresses; $\eta = T/\gamma$ is the wall tension to surface tension ratio, and $\Gamma = KH^2/\gamma$ is the wall elastance parameter. We examined steady-state solutions as a function of these parameters using lubrication analysis and the boundary element method.

These studies showed multiple-branch behaviour in the P_b – Ca relationship, where $P_b = P_b^*/(\gamma/H)$ is the dimensionless bubble pressure. Low Ca flows ($Ca \ll \min(1, (\Gamma^3/\eta)^{1/2})$) are dominated by the coupling of surface tension and elastic stresses. In this regime, P_b decreases as Ca increases owing to a reduction in the downstream resistance to flow, caused by the shortening of the section connecting the open end of the channel to the fully collapsed region. High Ca behaviour ($\max(1, (\Gamma^3/\eta)^{1/2}) \ll Ca \ll \eta$) is dominated by the balance between fluid viscous and longitudinal wall tension forces, resulting in a monotonically increasing P_b – Ca relationship. Increasing η or decreasing Γ reduces the Ca associated with the transition from one branch to the other. Low Ca streamlines show closed vortices at the bubble tip, which disappear with increasing Ca .

Start-up yield pressures are predicted to range from $1 \leq P_{yield}^*/(\gamma/L^*) \leq 2$, which is less than the minimum pressure for steady-state reopening, $P_{min}^*/(\gamma/L^*)$, where L^* is the upstream channel width. Since $P_{yield}^* < P_{min}^*$, the theory implies that low Ca reopening may be unsteady, a behaviour that has been observed experimentally. Our results are consistent with experimental observations showing that P_b^* in highly compliant channels scales with γ/L^* . In contrast, we find that wall shear stress scales with γ/H . These results imply that wall shear and normal stresses during reopening are potentially very large and may be physiologically significant.

1. Introduction

The lung consists of many generations of liquid-lined compliant tubes that conduct air to and from the alveoli – the primary site of gas exchange with the blood. Closure of small airways occurs in healthy adults at low lung volumes, in those with either emphysema or cystic fibrosis, and in infants with Respiratory Distress Syndrome (RDS). Such closure occurs owing to the formation of a liquid occlusion that hinders gas transport through the peripheral airways. Depending upon the duration of time these airways remain collapsed, such occlusion may be physiologically significant.

Infants at birth have lungs that are filled with liquid. The first several breaths force a bubble of air through the bronchial tree, allowing gas exchange to occur. However, infants with RDS lack significant quantities of surfactant, which raises the effort needed to inflate the lung, and leaves portions of the lung atelectatic. Although surfactant replacement therapy has been useful in treating this disease, recent data show that 5000 deaths/year in the United States may be attributed to RDS (Wiswell & Mediola 1993). It is important to understand the mechanisms used to open these airways in order to develop improved therapies for RDS.

In addition, patent airways may close when the lining fluid and/or walls become unstable, creating either a ‘meniscus occlusion’ that obstructs an otherwise air-filled bronchus, or ‘compliant collapse’, where fluid forces buckle the walls, which are held in apposition in a ‘ribbon-like’ configuration by the adhesive properties of the lining fluid (Greaves, Hildebrandt & Hoppin 1986; Kamm & Schroter 1989; Macklem 1971). It has been hypothesized that this closure is a consequence of the Raleigh instability of the airway/lining-fluid system. A number of theoretical studies analysing stability characteristics of this system have appeared in recent years (Johnson *et al.* 1991; Otis *et al.* 1993). Halpern & Grotberg (1992, 1993) showed that wall collapse and meniscus formation are a coupled event, and this coupling can significantly impact closure. A general review of the subject appears in Grotberg (1994). At present, no theoretical models of airway reopening exist that include fluid, elastic and surface-tension interactions.

In this paper, we analyse a model of a flexible-walled channel that is opened by a semi-infinite bubble that separates the walls, as shown in figure 1. This paradigm is based upon observations (Macklem, Proctor & Hogg 1970; Naureckas *et al.* 1994; Yap *et al.* 1994) that inflation of closed bronchi requires the peeling apart of opposing walls that are held in apposition in a ribbon-like configuration by the viscous lining fluid with fluid viscosity μ and surface tension γ . The reopening process is characterized by the velocity of the air bubble, U , and an applied bubble pressure, P_b^* , which is the pressure with respect to the external pressure surrounding the airway (including the peribronchial pressure).

This model has features that are common with two classical fluid mechanics investigations. The first is two-phase flow in either a rigid channel or tube, where a finger of air is forced through a viscous fluid contained between two narrowly spaced plates separated by a distance $2L^*$ or within a rigid tube of radius R^* (Saffman & Taylor 1958; Bretherton 1961; Park & Homsy 1984; Reinelt & Saffman 1985; Halpern & Gaver 1994). The fundamental parameter for these systems is the capillary number, $Ca = \mu U / \gamma$, which represents the relative magnitude of viscous to capillary stresses. Park & Homsy (1984) described the asymptotic regimes for this system. For $Ca \ll 1$, the bubble tip forms a capillary-statics region with a semi-circular (spherical for a tube) geometry. Owing to surface tension, this curved interface induces a pressure drop across an upstream transition region that connects the bubble tip to the uniform film

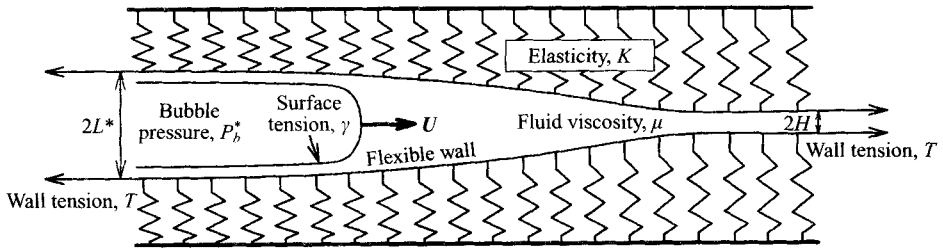


FIGURE 1. Schematic of the model system. Positive pressure, P_b^* forces a semi-infinite bubble through viscous fluid contained within a flexible-walled channel.

region far upstream. In the transition region, the fundamental balance is between surface tension and viscous forces. The pressure difference across the transition region sucks liquid around the bubble tip (in the laboratory frame) and helps to pull the bubble forward. However, in the limit of $Ca \rightarrow 0$, the film thickness in the transition region becomes infinitesimal and the pressure jump across the meniscus approaches γ/L^* for a channel or $2\gamma/R^*$ for a tube. This pressure jump can thus be considered to be a minimum pressure for initiating bubble motion, and thus we regard this to be a yield pressure, P_{yield}^* , for the system.

As Ca increases, the interfacial pressure jump increases monotonically. However, there is no reference pressure in the system for non-zero Ca , so P_b^* is not defined. This is a result of the rigid walls and parabolic flow field that extends to infinity. If the walls were finite in length, P_b^* could be defined with respect to the exit pressure. In this case, P_b^* would be time-dependent for a fixed U , owing to the shortening of the parabolic flow field downstream of the meniscus as the bubble moved forward, and the commensurate reduction of the total viscous pressure drop. So, the finite length rigid-walled system does not have a steady-state pressure-velocity relationship. In the present study, we will show that wall flexibility allows a steady-state response, by shortening the region where flows exist to a neighbourhood, albeit sometimes very long, of the bubble tip.

Another fundamental model that relates to the present study was investigated by McEwan & Taylor (1966), who examined the peeling of a flexible strip that was attached to a rigid wall by a viscous fluid that acts as an adhesive. In this example, there is no applied P_b^* ; the tape peels by application of wall tension, T , at a fixed angle. This reduces the pressure in front of the meniscus and sucks the meniscus forward. This mechanism exists in the airway reopening model; however, the angle is not predefined because the wall is a free surface that modifies its location as a function of the parameters in the problem.

Several experimental studies have been used to investigate the reopening system. The first was performed by Gaver, Samsel & Solway (1990), using compliant polyethylene tubes lined with viscous fluids. This study indicated that the fundamental lengthscale for reopening was based upon R^* , the upstream tube diameter. This study also indicated the presence of a yield pressure, $P_{yield}^* \sim 8\gamma/R^*$, that was necessary to initiate reopening. These studies were used to predict reopening pressures under a number of different disease states. More recent studies by Hsu, Strohl & Jamieson (1994), and Perun & Gaver (1995*a, b*) indicate that P_{yield}^* may be lower than original estimates, and is a function of the airway geometry. Experiments by Perun & Gaver (1995*b*) identified the importance of external wall stress on reopening. These studies showed that increased peribronchial stress can cause a commensurate decrease in the P_b^* necessary to open the airway.

Experimental investigations have been performed *in situ* by Naureckas *et al.* (1994) and Yap *et al.* (1994). These studies showed reopening pressures that were consistent with the estimates by Gaver *et al.* (1990). However, the studies by Yap *et al.* (1994) demonstrated that airway stability was a function of the tethering forces on the airway. When parenchymal tethering was small, airways would recollapse after reopening. This behaviour further indicates the significance of airway tethering forces in the system.

The goal of this study is to analyse a theoretical model of airway reopening. In this study, we investigate the fundamental behaviour resulting from the steady-state motion of a semi-infinite bubble that moves symmetrically between two compliant walls as shown in figure 1. We seek solutions for the bubble and airway geometry, and the relationship between the applied bubble pressure, P_b^* , and bubble velocity, U . In addition, we will calculate the interfacial surface velocities, the normal- and shear-stress distributions on the airway wall, and the flow patterns resulting from the bubble motion. We acknowledge that this model is a simplified representation of a true pulmonary airway reopening; however, we believe that this initial study will clarify the mechanical responses of the system, and thus provide an analytical basis for understanding airway reopening phenomena.

2. Formulation

2.1. Model description and assumptions

Figure 1 provides a schematic description of the airway model. As described above, in this model, a semi-infinite inviscid bubble of negligible density resides within a fluid of Newtonian viscosity μ , and constant density ρ . The interfacial tension, γ , is constant. The viscous fluid is constrained between membrane-like channel walls with constant longitudinal tension T supported elastically with a constant modulus of elasticity K . The wall has stress-free top and bottom positions defined at $y^* = \pm H$. Airway reopening occurs when a positive bubble pressure, P_b^* , is applied, which separates the walls to a distance $2L^* = 2(P_b^*/K + H)$, and forces the bubble to translate downstream (towards the right in figure 1) with a steady-state velocity U . In this model problem, we seek solutions that are steady-state in a frame fixed to the translating meniscus tip. We model this problem in Cartesian coordinates $\mathbf{x}^* = (x^*, y^*)$ fixed to the bubble tip, with velocity components $\mathbf{u}^* = (u^*, v^*)$. x^* represents a coordinate in the direction of bubble motion.

2.2. Scales

The governing equations are scaled as follows:

$$\mathbf{x}^* = H\mathbf{x}, \quad \mathbf{u}^* = U\mathbf{u}, \quad P^* = \frac{\gamma}{H}P. \quad (2.1)$$

The velocity scale, U , can be related to the two-dimensional flow rate of air into the system by $Q^* = 2U(L^* - H)$. The pressure scale, γ/H , represents a pressure drop due to an interfacial radius of curvature equal to H . Here, an asterisk represents a dimensional quantity of the associated scaled quantity. Another plausible lengthscale for this problem is L^* , the upstream wall separation. However, owing to its dependence upon P_b^* , this choice is not advisable in the mathematical formulation. Nevertheless, in §6.1 we show that in some cases this lengthscale (and the related pressure-scale γ/L^*) more appropriately describe the behaviour of the system.

2.3. Dimensionless governing equations and parameters

We assume slow viscous flow, and thus the Navier–Stokes equations for the liquid phase may be approximated by Stokes flow equations and continuity, which in scaled form are

$$\nabla P = Ca \nabla^2 \mathbf{u}, \quad \nabla \cdot \mathbf{u} = 0, \quad (2.2)$$

where the capillary number, $Ca = \mu U / \gamma$ represents the ratio of viscous to capillary stresses and can be considered a dimensionless bubble tip velocity.

The dimensionless interfacial stress conditions are given by

$$\boldsymbol{\sigma}^{(2)} \cdot \mathbf{n} = -(\kappa_{int} - P_b) \mathbf{n} \quad \text{at} \quad y = y_m, \quad (2.3)$$

where $y = y_m$ represents the meniscus position, and $\mathbf{n} = (n_x, n_y)$ is the viscous fluid outward-facing normal. The interfacial surface curvature is defined as $\kappa_{int} = \nabla_s \cdot \mathbf{n}$, where $\nabla_s = (\mathbf{I} - \mathbf{nn}) \cdot \nabla$ is the surface divergence vector. $\boldsymbol{\sigma}^{(2)} = -P\mathbf{I} + Ca(\nabla \mathbf{u} + \nabla \mathbf{u}^T)$ is the airway lining fluid stress tensor, and we have assumed that the bubble viscosity is negligible, so the stress tensor for the bubble is $\boldsymbol{\sigma}^{(1)} = -P_b \mathbf{I}$. In this model, we have excluded surface tension variation along the interface that could be caused by a non-uniform surfactant distribution. For this reason, interfacial shear stresses cannot be sustained.

We assume that the wall is massless and inextensible, and is supported elastically in only the y -direction with springs allowed to translate freely in the x -direction. In dimensionless form, the wall stress condition for the bottom wall is thus

$$\mathbf{n} \cdot \boldsymbol{\sigma}^{(2)} \cdot \mathbf{n} = -\eta \kappa_{wall} + \Gamma(y+1)n_y \quad \text{at} \quad y = y_w, \quad (2.4)$$

where $y = y_w$ defines the wall position, $y_w = -1$ is the bottom wall stress-free position, and $\kappa_{wall} = \nabla_s \cdot \mathbf{n}$ is the wall curvature. $\eta = T/\gamma$ is the dimensionless wall tension, and $\Gamma = KH^2/\gamma$ represents the dimensionless wall stiffness. The external pressure is the reference pressure for the system. Limitations related to approximations used to derive this relationship are described in §6.4.

Under steady-state conditions with respect to the meniscus tip frame of reference, wall disturbances propagate as a travelling-wave at the same rate as the meniscus tip. This implies that

$$u = n_x^2 - 1, \quad v = n_x n_y \quad \text{at} \quad y = y_w. \quad (2.5)$$

We assume that in the laboratory frame, no flows exist as $x^* \rightarrow \pm \infty$. Also, global conservation of mass implies that the film thickness as $x \rightarrow \pm \infty$ must equal H . In the meniscus frame of reference, the dimensionless downstream conditions are therefore:

$$\left. \begin{array}{l} \mathbf{u} \rightarrow -\mathbf{e}_x \\ y_w \rightarrow \pm 1 \end{array} \right\} \quad \text{as} \quad x \rightarrow \infty, \quad (2.6)$$

where $\mathbf{e}_x = (1, 0)$. Far upstream of the meniscus, the applied bubble pressure results in a wall separation of $2L^* = 2(P_b^*/K + H)$. In dimensionless form the upstream conditions are:

$$\left. \begin{array}{l} \mathbf{u} \rightarrow -\mathbf{e}_x \\ y_m \rightarrow \pm \frac{P_b}{\Gamma} \\ y_w \rightarrow \pm \left(\frac{P_b}{\Gamma} + 1 \right) \end{array} \right\} \quad \text{as} \quad x \rightarrow -\infty. \quad (2.7)$$

Our goal is to determine the functional relationship between P_b and the parameters Ca , Γ , and η that describe the physical properties of the system. To do so, we seek the solution of the double free-surface boundary-value problem described by (2.2)–(2.7). This solution will provide the wall and interface shapes as well as the velocity and stress distribution in this problem. We solve this problem using two approaches: an analytical lubrication theory analysis, and a computational approach using the boundary-element method. These methods allow us to describe this system over a large range of the parameters.

2.4. Macroscopic momentum balance analysis

To understand the behaviour of the system, it is instructive to examine a control-volume analysis of the x -component of momentum. In this analysis, consider a control volume moving with constant velocity U , surrounding the bubble tip with vertical boundaries far upstream and downstream of the tip. Let the boundaries connecting these segments trace the inside of the wall, in contact with the fluid. Far downstream the walls are in their stress-free locations ($y_w = \pm 1$), and upstream the wall is displaced to a constant location defined by $P_b(y_w = \pm L)$, where $L = L^*/H = P_b/\Gamma + 1$. Since the flows through the left- and right-hand sides of the control volume are identical, and the downstream pressure is zero,

$$P_b = \frac{1}{L} \left(\int_{-\infty}^{\infty} (\tau_x)_{wall} ds + 1 \right). \quad (2.8)$$

Here, $(\tau_x)_{wall}$ is the x -component of stress on the wall, $(\tau_x)_{wall} = -(\mathbf{e}_x \cdot \boldsymbol{\sigma}^{(2)} \cdot \mathbf{n})$, where \mathbf{n} is the fluid outward-facing normal. Clearly, $(\tau_x)_{wall}$ depends upon the flow field, and thus is a function of Ca , η and Γ . This behaviour will be examined below. Also, Γ influences the magnitude of P_b by setting the upstream channel width. Reducing Γ results in an increase in L , reducing the magnitude of P_b assuming $(\tau_x)_{wall}$ is held constant. Below we describe the relationships between the flow parameters and the behaviour of the system.

3. Methods of solution

Two different approaches to the analysis of this problem are used. Lubrication theory is described in §3.1, and the boundary-element method is described in §3.2. The solutions provided by each method contribute novel insights concerning the physics of the bubble progression through the flexible channel, as will be discussed in §5.

3.1. Lubrication theory

Lubrication theory is used to analyse this system for a number of reasons. First, this method describes the salient physics at low Ca , and thus provides important insight into this regime. Secondly, since the solution is asymptotically accurate as $Ca \rightarrow 0$, it provides important validation of the boundary-element approach. At the ends of the domain, lubrication theory is justifiable because variations of the flow field in the x -direction are smaller than variations in the y -direction. This occurs upstream of the bubble tip (region I) because the thickness of the liquid layer is small compared to the axial lengthscale of the bubble, and far downstream of the tip (region II) because the channel walls are almost parallel to each other. An arc-length formulation of the bubble-tip region is used to match regions I and II to provide a complete solution. The accuracy of the arclength formulation is described below. The lubrication approxi-

mations for regions I and II are important to the boundary-element formulation because they are used as end-conditions for the boundary-element solution in order to truncate the boundary-element domain, as discussed in §3.2. In addition, the lubrication approximations of regions I and II are important to the scaling arguments given in §5.

Region I (upstream region)

We assume that fluid inertia is negligible and that the fluid is Newtonian and incompressible. Since away from the tip the film thickness is much smaller than the length of the bubble, the dimensionless momentum equations (2.21) in the horizontal and vertical directions

$$\frac{\partial p}{\partial x} = Ca \frac{\partial^2 u}{\partial y^2}, \quad \frac{\partial p}{\partial y} = 0, \quad (3.1 a, b)$$

where p is the fluid pressure and u is the horizontal fluid velocity. At the air-liquid interface, $y = y_m = f(x)$, the interfacial tangential and normal stress conditions (2.3) are approximated as:

$$\frac{\partial u}{\partial y} = 0, \quad p - p_b = \frac{\partial^2 f}{\partial x^2}. \quad (3.2 a, b)$$

At the wall, $y = y_w = h(x)$, the normal stress condition (2.4) reduces to:

$$p = \Gamma(h-1) - \eta \frac{\partial^2 h}{\partial x^2}. \quad (3.3)$$

The velocity field is determined by integrating (3.1 *a*) twice with respect to y . By using the fact that the dimensionless axial flow rate is given by

$$Q = \int_f^h u \, dy = -1, \quad (3.4)$$

the following expression for the pressure gradient is obtained:

$$\frac{\partial p}{\partial x} = \frac{3Ca}{(h-f)^3} (1-h+f). \quad (3.5)$$

A system of ordinary differential equations for h and f is then obtained by substituting the linear wall equation (3.3) into (3.2 *b*) and (3.5):

$$\Gamma h' - \eta h''' = \frac{3Ca}{(h-f)^3} (1-h+f), \quad (3.6 a)$$

$$f'' + \eta h'' = \Gamma(h-L), \quad (3.6 b)$$

where $h' = dh/dx$ and $f' = df/dx$. In this transition region, both viscous forces and surface-tension forces are important. As $x \rightarrow -\infty$, both interfaces become uniform, $h \rightarrow L$ and $f \rightarrow L-1$, and $P_b = \Gamma(L-1)$. A rescaling of x , such that $x = (3Ca)^{-1/3} \bar{x}$ is applied when solving the above equations numerically. This scaling is based on the rigid tube result in the limit of $Ca \rightarrow 0$, and is appropriate for the transition region between the constant film thickness region and a constant curvature 'capillary-statics' region (Landau & Levich 1942; Bretherton 1961; Park & Homsy 1984). For the rigid-

channel case, h is constant and (3.6) reduces to the Landau–Levich equation for the film thickness, $h-f$, (equation (12), Landau & Levich 1942). This equations is relevant to a wide variety of capillary-dominated flows. This scaling is still useful even though we do not employ the constant curvature condition in the arc-length formulation of the bubble tip described below. Appendix A describes the linearization of this system for use in determining the upstream condition for region I.

Region II (downstream region)

The governing equation for the wall position, h , in the fluid-filled region is obtained by setting $f = 0$ in (3.6a) and is therefore given by

$$\eta h''' - \Gamma h' = 3Ca \frac{(h-1)}{h^3}, \quad (3.7)$$

with $h \rightarrow 1$ as $x \rightarrow \infty$. Appendix A provides the solution to the linearized form of this equation for use as a boundary condition for region II.

Note that for $\eta = 0$, h is purely decaying, but there is only one eigenfunction. In this case, the wall shape is determined by the analytic solution

$$x = \frac{\Gamma}{3Ca} \left(\ln \left(\frac{1-h_0}{1-h} \right) + h_0 - h + \frac{1}{2}(h_0^2 - h^2) + \frac{1}{3}(h_0^3 - h^3) \right), \quad (3.8)$$

where h_0 is the wall displacement at the bubble-tip location.

Arc-length formation

In the bubble-tip region, it is valuable to use the arclength of either the air–liquid interface or the wall as the independent variable. This coordinate transformation permits the interfacial and wall curvature to be expressed exactly, and smoothly incorporates the bubble tip into the model. This approach includes all the terms that are important in the lubrication theory regions and capillary statics region, and thus eliminates the need to truncate the lubrication domain and fit a semi-circular cap to complete the bubble tip, as was done by Bretherton (1961) and Park & Homsy (1984) in their lubrication analyses of bubble motion in a rigid channel. This method was successfully used to study the motion and deformation of red blood cells through liquid filled capillary tubes (Halpern & Secomb 1989, 1991) and to study viscous fluid displacement by long air bubbles (Ratulowski & Chang 1990).

Halpern & Secomb (1991) have shown that although the arc-length formulation uses lubrication approximations in regions where the gap is not uniformly narrow, the pressure drop and speed can be accurately evaluated. This is true because errors due to lubrication approximations where film thicknesses are large are relatively small in comparison to the total pressure drop in the system in regions where film thickness is small. Comparison of solutions of semi-infinite bubble motion in a rigid channel using these techniques with solutions by Halpern & Gaver (1994) using the boundary-element method show that the arc-length formulation extends the accuracy of the lubrication solutions to $Ca \sim 0.1$. In the flexible-walled system the accuracy may extend to even larger Ca under values of Γ and η where large pressure drops occur away from the bubble tip.

We define θ to be the angle between the tangent to the air–liquid interface and the horizontal, ϕ to be the angle between the tangent to the wall and the horizontal, and s_1 and s_2 to be respectively the arc lengths measured along the air–liquid interface and

wall. Since $ds_1/ds_2 = \cos \phi / \cos \theta$, the governing equations in region I can be expressed in terms of only one independent variable, s_1

$$\frac{dx}{ds_1} = \cos \theta, \quad (3.9a)$$

$$\frac{df}{ds_1} = -\sin \theta, \quad (3.9b)$$

$$\frac{d\theta}{ds_1} = -(p - p_b), \quad (3.9c)$$

$$\frac{dp}{ds_1} = \frac{3Ca}{(h-f)^3} (1-h+f) \cos \theta, \quad (3.9d)$$

$$\frac{dh}{ds_1} = -\tan \phi \cos \theta, \quad (3.9e)$$

$$\frac{d\phi}{ds_1} = \frac{1 \cos \theta}{\tau \cos \phi} (p - \Gamma(h-1) \cos \phi). \quad (3.9f)$$

Note that 3.9(c) is the normal stress condition at the air-liquid interface (3.2b), and (3.9b, f) arise from the wall equation (3.3). Equation (3.9d) shows that as the film thickness $(h-f)$ becomes large, the pressure gradient decreases in proportion to $(h-f)^{-2}$. At low Ca , (3.9d) is thus consistent with the constant curvature assumption of the capillary-statics regime used by Bretherton (1961) and Park & Homsy (1984).

Likewise, the equations in region II are given by:

$$\left. \begin{aligned} \frac{dx}{ds_2} &= \cos \phi, \\ \frac{dh}{ds_2} &= -\sin \phi, \\ \frac{d\phi}{ds_2} &= \frac{1}{\tau} (p - \Gamma(h-1) \cos \phi), \\ \frac{dp}{ds_2} &= \frac{3Ca}{h^3} (1-h) \cos \phi. \end{aligned} \right\} \quad (3.10)$$

Equations (3.9) and (3.10) are solved simultaneously using a finite-difference method. The required boundary conditions are obtained by linearizing the governing equations at $x \rightarrow \pm \infty$ as described in Appendix A, and by applying matching conditions on h , ϕ , p , f ($f=0$) and θ ($\theta = \frac{1}{2}\pi$) at the bubble tip ($x=0$) where regions I and II meet. Hence, for given values of Ca , Γ and η , we can uniquely determine the wall and air-liquid interface, h and f . P_b is determined from the far-upstream wall position using (3.3).

3.2. Boundary element method

The solution for the velocity field resulting from Stokes flow is obtained in terms of single- and double-layer potentials by taking Fourier transforms of equation (2.2) and applying Green's theorem (Ladyzhenskaya 1963):

$$\mathbf{u}_k(\mathbf{x}) = \int_S \mathbf{T}_{ik}(\mathbf{x}, \mathbf{y}) \mathbf{u}_i dS_y - \frac{1}{Ca} \int_S \mathbf{U}_{ik}(\mathbf{x}, \mathbf{y}) \tau_i dS_y, \quad (3.11)$$

where

$$\left. \begin{aligned} U_{ik}(x, y) &= -\frac{1}{4\pi} \left\{ \delta_{ik} \log|x-y| - \frac{(x_i - y_i)(x_k - y_k)}{|x-y|^2} \right\}, \\ T_{ik}(x, y) &= -\frac{1}{\pi} \frac{(x_i - y_i)(x_j - y_j)(x_k - y_k)}{|x-y|^4} n_j(y). \end{aligned} \right\} \quad (3.12)$$

S represents the boundary surface and $\tau_i = \sigma_{ij} n_j$ with i, j equal to 1 (x -direction) or 2 (y -direction). As \mathbf{x} approaches a point on the boundary surface, the solution of (3.11) becomes:

$$C_{ki} \mathbf{u}_i(\mathbf{x}) = \int_S T_{ik}(\mathbf{x}, \mathbf{y}) \mathbf{u}_i dS_y - \frac{1}{Ca} \int_S U_{ik}(\mathbf{x}, \mathbf{y}) \tau_i dS_y, \quad (3.13)$$

where $\mathbf{x} \in S$, and the tensor C_{ki} accounts for stress discontinuities at the surface. $C_{ki} = \frac{1}{2} \delta_{ki}$ if the boundary is smooth, but has a more complicated structure if the domain has corners (Brebbia & Dominguez 1989). Equation (3.13) is solved numerically by discretizing the boundary into N 3-point (quadratic) elements, so that

$$C_{ki} \mathbf{u}_i(\mathbf{x}) - \sum_{j=1}^N \int_{S_j} T_{ik}(\mathbf{x}, \mathbf{y}) \mathbf{u}_i dS_y = -\frac{1}{Ca} \sum_{j=1}^N \int_{S_j} U_{ik}(\mathbf{x}, \mathbf{y}) \tau_i dS_y, \quad (3.14)$$

where \mathbf{u} and τ are discretized along the domain, and represented by quadratic polynomials.

Equations (3.14) is represented by a system of linear equations

$$\mathbf{H} \mathbf{w} = \mathbf{G} \mathbf{t}, \quad (3.15)$$

where \mathbf{H} and \mathbf{G} are, respectively, $4N \times 4N$ and $4N \times 6N$ matrices, and $w_{2j-1} = u_j$, $w_{2j} = v_j$, $t_{2j-1} = \tau_{xj}$, $t_{2j} = \tau_{yj}$ for $j = 1, 2, \dots, 2N$. Matrix \mathbf{G} is made larger than \mathbf{H} to allow the stress vector to have two distinct values at corner points because of two possible orientations of the normal vector. This is particularly useful at corner points (see Appendix B). The elements of \mathbf{H} and \mathbf{G} are computed using a 10-point regular Gaussian quadrature if \mathbf{x} does not coincide with one of the node points of S_j . Otherwise a 10-point logarithmic quadrature is used to evaluate those portions of the integrals in (3.14) that contain the logarithmic singularity. The diagonal coefficients of \mathbf{H} are computed indirectly by imposing a uniform flow in both the x - and y -directions. We then apply the boundary conditions and rearrange the system so that $\mathbf{A} \mathbf{z} = \mathbf{f}$, where \mathbf{A} is a $4N \times 4N$ matrix, \mathbf{z} is a $2N$ vector containing the unknown velocities and stresses and \mathbf{f} contains the known stress or velocity information. This system is solved using Gaussian elimination with partial pivoting.

Domain truncation

It is not practical to extend the boundary-element domain to be large enough to satisfy the end conditions provided by (2.6) and (2.7). For this reason, the domain is truncated to a neighbourhood of the bubble tip, and we attach lubrication approximation conditions on the left- and right-hand boundaries. Since the problem is symmetric about the centreline, we analyse only the bottom half of the domain, as shown in figure 2. Segments A , B , C , D and E represent the boundary segments. Fluid stresses and velocities along domain segments B and E are provided by regions 1 and 2 lubrication approximations, respectively. These approximations are calculated to match the wall position and curvature at ends of the domain (x_{right} and x_{left}). To couple the lubrication solutions to the boundary-element domain, the cubic splines that

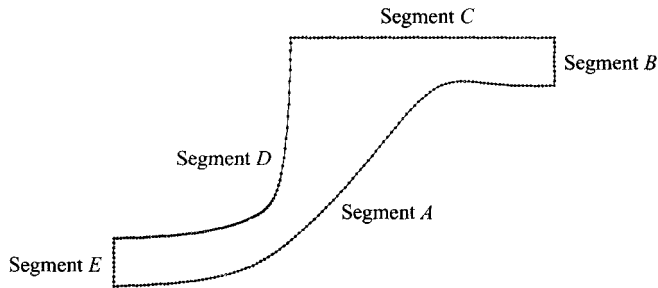


FIGURE 2. Description of the half-domain used for the boundary-element computations.

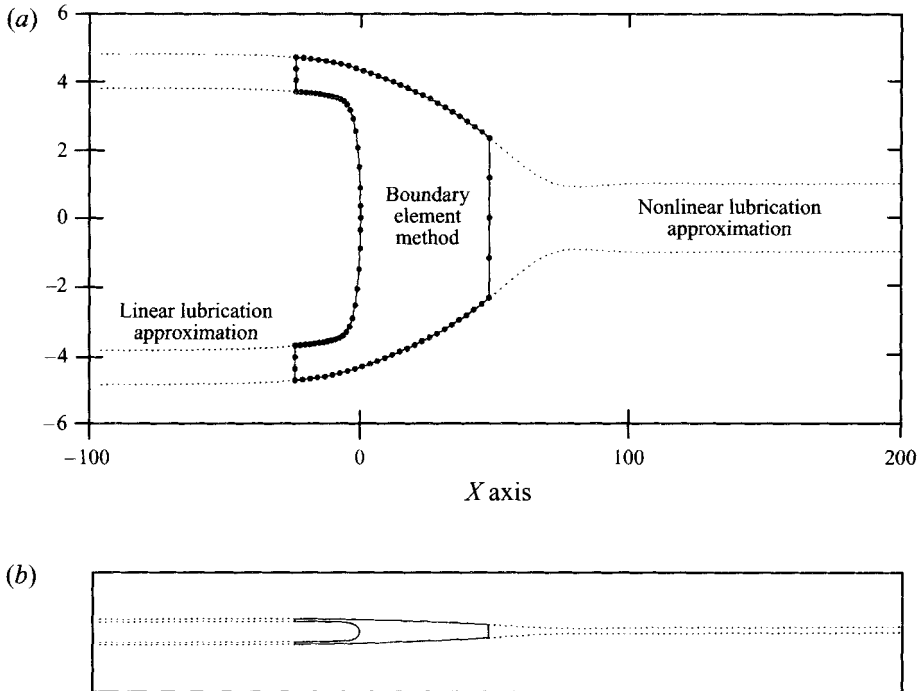


FIGURE 3. (a) Description of the coupling of the boundary-element domain to lubrication theory end-conditions; $Ca = 0.2$, $\Gamma = 1.0$, $\eta = 250$; (b) diagram indicating the physical aspect ratio for this system.

define the wall in the boundary-element regime use specified end-conditions that match to the lubrication wall slope as provided by (A 4) and the solution of (3.7). Iteration of the end-wall conditions is incorporated into the wall position iteration described below. Figure 3(a) demonstrates the coupling between the boundary element and lubrication approximation domains. Figure 3(b) shows these profiles in the physical aspect ratio. Extending the boundary-element domain beyond the neck region is not necessary, although doing so improves the rate of convergence to the steady solution.

Iteration procedure

Equation (3.15) relates the stresses (τ) and velocities (\mathbf{u}) on the domain. A steady-state meniscus shape exists when boundary conditions (2.3)–(2.5) are satisfied with

$$\mathbf{u} \cdot \mathbf{n} = 0 \quad \text{at} \quad y = y_m(x, t). \quad (3.16)$$

Given an initial domain, the known values of τ on the air–liquid interface are given by

(2.3) and the values of \mathbf{u} on the wall are provided by (2.5). The solution of (3.15) provides the unknown interfacial velocities and wall stresses. To satisfy the remaining boundary conditions, an iterative procedure is used to determine the correct domain shape and P_b that satisfy (2.4) and (3.16) for fixed values Ca , η and Γ .

The iteration process sequentially modifies the air–liquid interface shape, P_b , and the wall shape to find a steady-state solution. Given Ca , η and Γ , an initial domain and an estimate of P_b , the interface is modified using the kinematic boundary condition,

$$\frac{DY}{Dt} \cdot \mathbf{n} = \mathbf{u} \cdot \mathbf{n}, \quad (3.17)$$

where $\mathbf{Y} = (x_m(s, t), y_m(s, t))$ is the interfacial position vector, s is the arclength, and t is time, but is used as an iteration parameter to find the steady-state response. This is solved using the Adams–Bashforth method.

Periodically, a Newton’s method is used to adjust P_b so that the bubble tip remains stationary, retaining the bubble-tip frame of reference. For a given wall shape, the interface is assumed to be steady-state when $\max(\mathbf{u}_{interface} \cdot \mathbf{n}) < 1 \times 10^{-3}$. This interface is used to calculate wall stresses while we apply Newton’s method to reposition the wall to satisfy (2.4). After wall relocation, the meniscus may no longer satisfy the steady-state criterion, and thus the meniscus iteration (3.17) is repeated. Iteration continues until $\max(\mathbf{u}_{interface} \cdot \mathbf{n}) < 1 \times 10^{-3}$ with a maximum dimensionless wall stress deviation $< 1 \times 10^{-3}$. Reducing the convergence criteria by a factor of 10 results in only a small change in the final solution ($\sim 1\%$ change in P_b), and therefore these criteria are deemed suitable for calculating the steady-state solution. Implementation considerations regarding the accurate administration of the boundary-element method to this problem are discussed in Appendix B.

4. Results

The computations performed on this system using the boundary-element method and lubrication theory span the parameters Ca , Γ and η . We regard as a basic state the following dimensionless parameter set: $Ca = 0.5$, $\eta = 100$ and $\Gamma = 0.5$. When investigating the influence of a particular dimensionless parameter, we will compare the behaviour to that of this basic state with the remaining parameters held constant. In figures presented below, we explore each of the parameters to demonstrate its influence on specific characteristics of the system. These are the dimensionless bubble pressure, $P_b = P_b^*/(\gamma/H)$; the dimensionless radius of curvature at the bubble tip, $R_{tip} = R_{tip}^*/H$; the dimensionless interfacial pressure drop at the bubble tip, $\Delta P = \Delta P^*/(\gamma/H)$, and the dimensionless upstream channel width, $L = L^*/H$. In addition, for unique values of the spanned parameter, we demonstrate specific domain shapes and wall shear and normal stresses.

The influence of Ca

The influence of Ca is shown in figures 4(a–d), 5(a–d) and 6(a–b). Figures 4(a)–4(d) show the general behaviour of the system over $0.05 \leq Ca \leq 2.0$ with $\eta = 100$ and $\Gamma = 0.5$. From these figures, the most striking response of the system is the non-monotonic relationship between P_b and Ca , shown in figure 4(a). For Ca small ($Ca < 0.3$), an increase in Ca requires a decrease in P_b ; however, for $Ca > 0.3$, an increase in Ca is accompanied by a rise in P_b . Lubrication theory (dotted line) predicts this turnaround, but underestimates the rate of increase of P_b . The multi-branch behaviour of the P_b – Ca relationship is discussed in detail in §5, below.

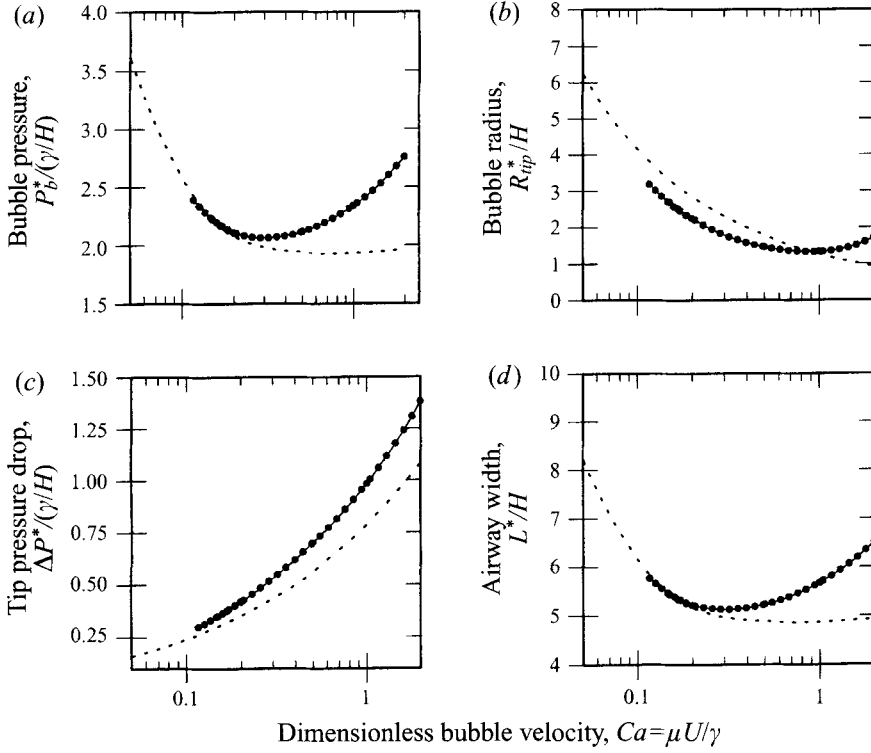


FIGURE 4. The influence of $Ca = \mu U / \gamma$ on the reopening behaviour. $\Gamma = KH^2 / \gamma = 0.5$, $\eta = T / \gamma = 100$: \cdots , lubrication theory; $\bullet\bullet\bullet$, boundary-element method.

Figure 4(b) shows that the boundary-element method predicts a minimum R_{tip} at $Ca \sim 0.9$. However, lubrication theory predicts that R_{tip} decreases monotonically with Ca in the range examined. Figure 4(c) shows that the system's response results in a monotonically increasing interfacial pressure drop. This suggests that the interfacial pressure drop creates a driving force for meniscus motion by 'sucking' the bubble forward. The fact that ΔP increases monotonically while R_{tip} at first decreases and then increases indicates the significance of the viscous normal stress when $Ca \sim O(1)$. Finally, figure 4(d) shows that the upstream channel width is a non-monotonic function of Ca , a response that is directly related to P_b . This figure shows that the upstream wall deflects to a width that is at least 5 times the downstream wall displacement width.

Figures 5(a)–5(d) demonstrate the influence of Ca on the domain shape for $Ca = 0.1, 0.2, 0.5$ and 1.0 , with $\eta = 100$ and $\Gamma = 0.5$. These figures clearly show that increasing Ca causes a more radical wall deflection. Furthermore, the wall 'necks' inward downstream of the meniscus tip, and is deflected past the stress-free location before returning to $y_w = \pm 1$ far downstream. This necking behaviour becomes more prevalent as Ca increases. Finally, increasing Ca results in the upstream portion of the bubble having a longer region of non-zero slope.

Dimensionless wall normal (τ_n) and shear (τ_s) stresses are shown in figures 6(a) and 6(b). Note that $\tau_s \sim (\tau_x)_{wall}$ in (2.8), owing to the small wall slope, and thus can be used to infer the influence of stress on the reopening pressure. The relationship between Ca and τ_n is shown in figure 6(a). In the thin-film region of the bubble, the viscous lining has virtually a uniform velocity, so $\tau_n \sim P_b$. Far downstream, the wall approaches the

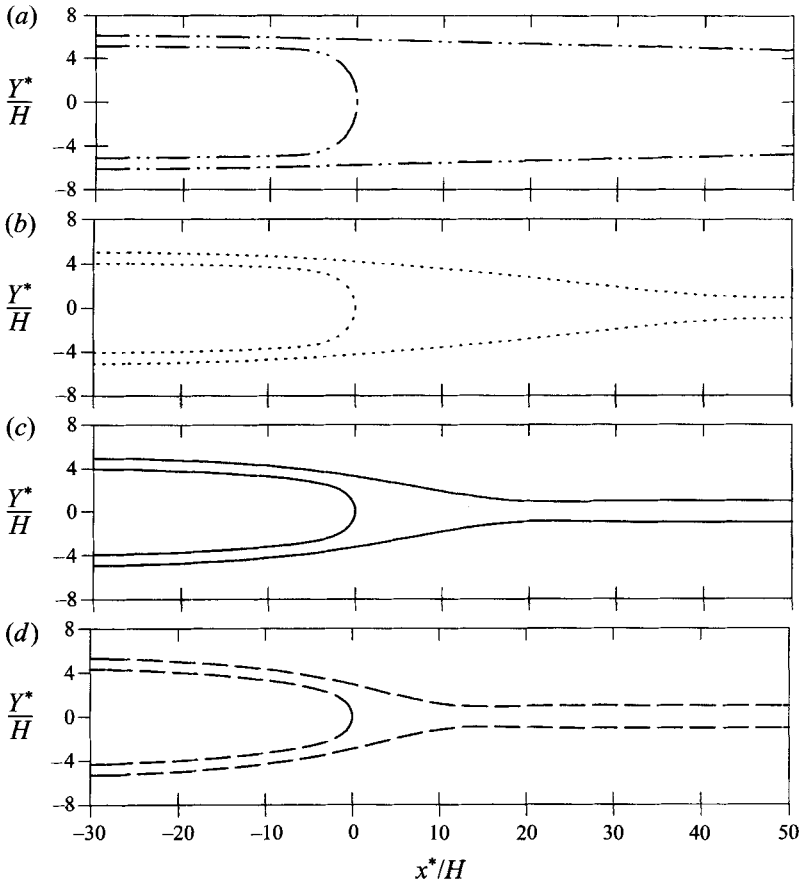


FIGURE 5. The influence of $Ca = \mu U/\gamma$ on the domain. $\Gamma = KH^2/\gamma = 0.5$, $\eta = T/\gamma = 100$;
 (a) $Ca = 0.1$, (b) $Ca = 0.2$, (c) $Ca = 0.5$, (d) $Ca = 1.0$.

stress-free location, and $\tau_n \sim 0$. For $Ca = 0.2$ and 0.5 , P_b is nearly identical, indicating opposite branches of the data in figure 4(a). At the bubble tip ($x = 0$), the interfacial pressure drop (figure 4c) results in a decrease of τ_n . Viscous stresses further reduce τ_n downstream of the bubble at a rate that increases with Ca . In concert with the interfacial pressure drop, this stress gradient is the driving force for fluid motion in the system. In the region downstream of the bubble, wall curvature induces a region where $\tau_n < 0$ owing to wall curvature influencing the wall-stress condition (2.4). This pulls the wall inward from its equilibrium position, creating the necking behaviour shown clearly in figures 5(c) and 5(d). Note that the stress minimum for $Ca = 1.0$ has a magnitude that is equivalent to the stress maximum. For cases where $Ca > 1$, the location of the largest stress will occur downstream of the bubble tip, so the P_b may not accurately reflect the magnitude of the normal stress in the system.

The influence of Ca on the dimensionless wall shear stress, τ_s , is shown in figure 6(b). Far upstream and downstream $\tau_s \rightarrow 0$, since the velocity field is essentially uniform in those regions (the fluid is static in the laboratory frame). τ_s is substantial in the transition between these two regions, with $\tau_s > 0$ near the bubble tip and $\tau_s < 0$ further downstream. The region with $\tau_s < 0$ corresponds to the site where the wall necks inward ($\tau_n < 0$). In the laboratory frame, this would result in fluid moving in a direction opposite to that of the bubble in the vicinity downstream of the bubble tip.

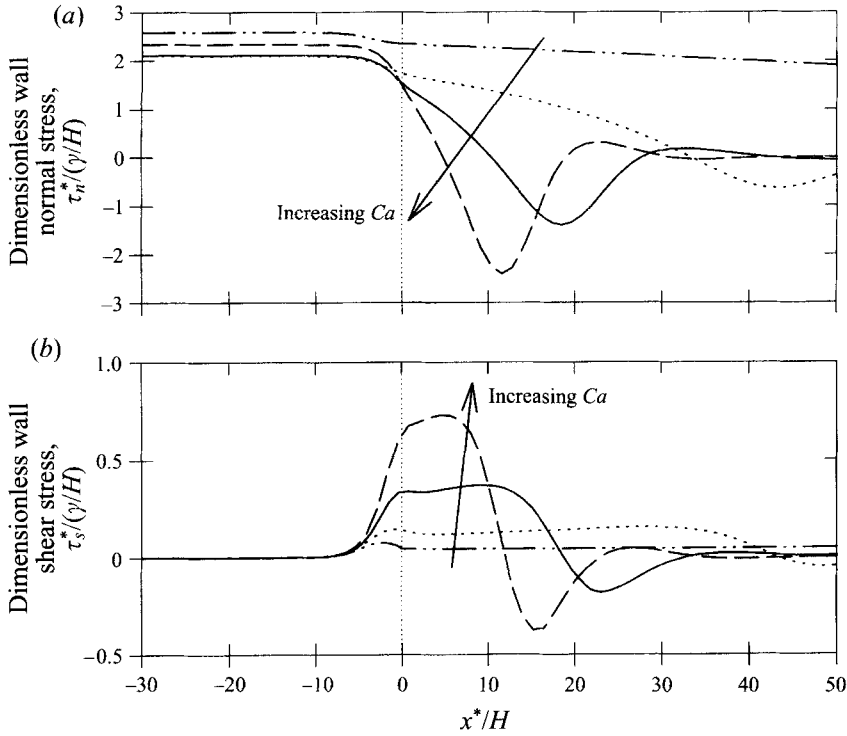


FIGURE 6. The influence of $Ca = \mu U/\gamma$ on wall stresses. $\Gamma = KH^2/\gamma = 0.5$, $\eta = T/\gamma = 100$. $-\cdot-\cdot-$, $Ca = 0.1$; \cdots , $Ca = 0.2$; $---$, $Ca = 0.5$; $----$, $Ca = 1.0$. (a) Dimensionless normal stress, $\tau_n^*/(\gamma/H)$; (b) dimensionless shear stress, $\tau_s^*/(\gamma/H)$.

Such retrograde fluid motion was reported in experiments by Gaver *et al.* (1990). This figure also shows that the magnitude of τ_s increases with Ca ; however, the length of the flow domain in which τ_s is large decreases with increasing Ca . This influences the

$$\int_{-\infty}^{\infty} (\tau_x)_{wall} ds$$

in (2.8), and relates significantly to the transition from the left-hand to right-hand branches of figure 4(a). This will be discussed in detail in §5.3, below.

The influence of η

Figures 7(a–d), 8(a–c) and 9(a, b) illustrate the influence of the wall tension parameter, η , on the behaviour of the reopening system with $Ca = 0.5$, $\Gamma = 0.5$. Figure 7(a)–(d) show the behaviour of specific characteristics over $10 \leq \eta \leq 250$, while figures 8 and 9 demonstrate domain shape and stress behaviour for $\eta = 10, 100$ and 250. Figure 7(a) indicates that in this range of Ca (the right-hand branch of the P_b – Ca relationship shown in figure 4a), increasing η requires that P_b increase. In addition, R_{tip} decreases slightly as η increases (figure 7b). Together, these result in a small increase in the pressure drop across the meniscus tip, ΔP , as shown in figure 7(c). Finally, figure 7(d) shows that the increased P_b required with larger η results in larger upstream wall deflections.

Figures 8(a–c) and 9(a, b) put the results of figures 7(a)–7(d) in context, and explain why increasing η necessitates larger P_b . Figure 8 shows that the major influence of

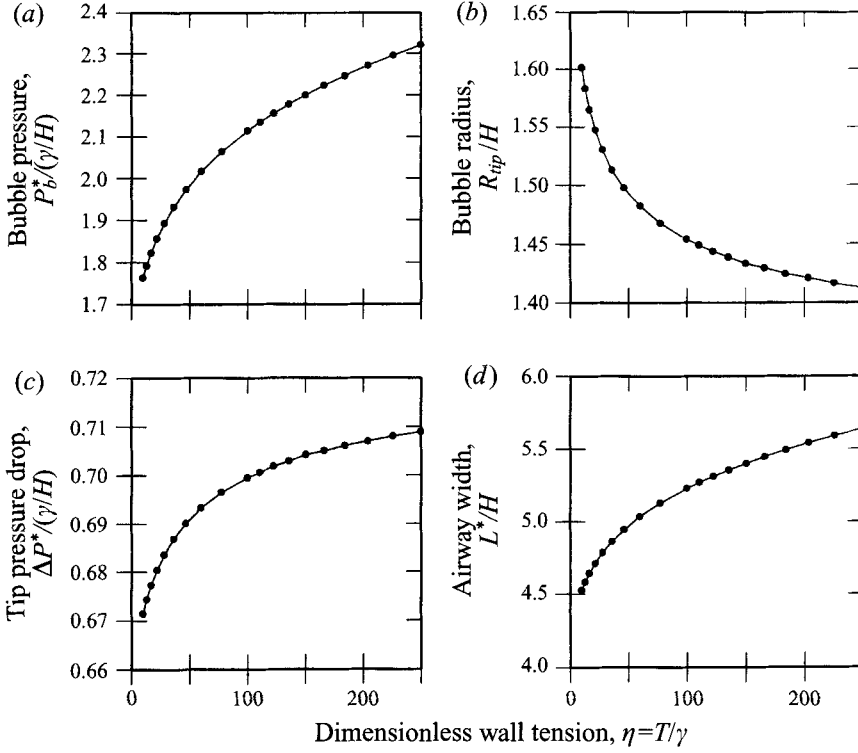


FIGURE 7. The influence of $\eta = T/\gamma$ on the reopening behaviour. $\Gamma = KH^2/\gamma = 0.5$, $Ca = \mu U/\gamma = 0.5$.

increasing wall tension is to stretch the transition from the bubble to completely collapsed section. This indicates that increasing η extends the region of significant flow downstream of the meniscus tip. The bubble tip geometry is not greatly influenced by the increase in η , but the upstream wall deflection increases slightly. This increased deflection is due to the larger P_b .

Figure 9(a) shows that τ_n is influenced by η . First, the upstream τ_n ($\sim P_b$) increases with increasing η , indicating that wall tension retards reopening. This result should be compared to that found by McEwan & Taylor (1966), who showed in their tape peeling studies that increased wall tension increased the rate of meniscus progression. However, in those models the upstream angle of incidence of the wall was held constant. In our model, the wall angle is not held constant; increasing η reduces the angle of incidence. Downstream of the bubble tip, $\tau_n < 0$ owing to wall curvature. The magnitude of this negative stress (essentially a downstream suction pressure) increases with increasing η , and can be larger than P_b . However, the location of the τ_n minimum moves downstream with increasing η , and the normal stress gradient is not greatly influenced by η . This indicates that the pressure gradient is not greatly influenced by η . So, this behaviour cannot explain the increase in P_b related to an increase in η .

Figure 9(b) demonstrates the influence of η on τ_s , and resolves the increase in P_b required with increasing η . This figure shows that the extremum values of the shear stress are independent of η , but the range of non-zero τ_s extends further downstream as η increases. This increases the

$$\int_{-\infty}^{\infty} (\tau_x)_{wall} ds$$

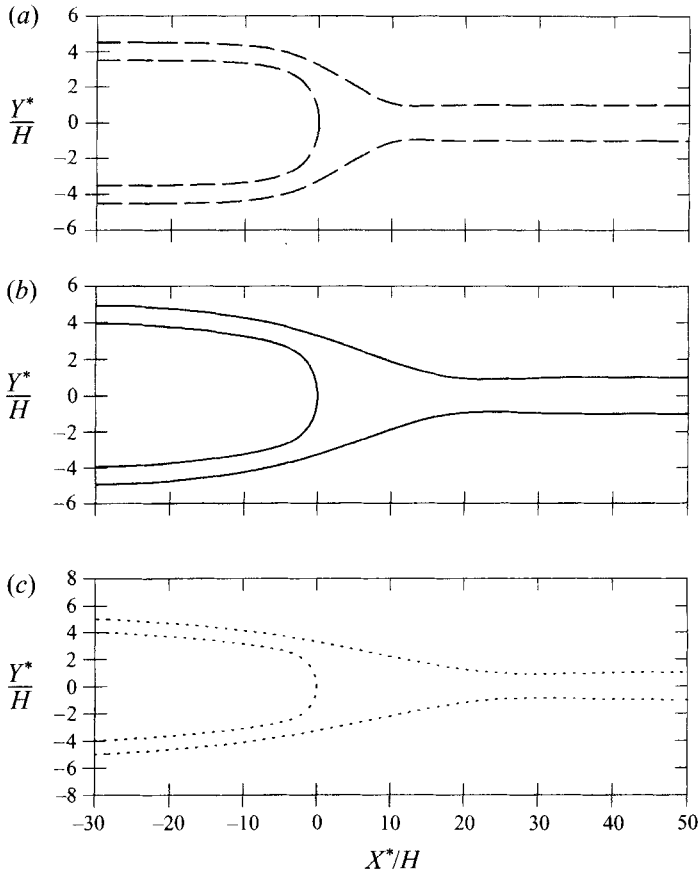


FIGURE 8. The influence of $\eta = T/\gamma$ on the domain. $\Gamma = KH^2/\gamma = 0.5$.
 $Ca = \mu U/\gamma = 0.5$ (a) $\eta = 10$, (b) $\eta = 100$, (c) $\eta = 250$.

in (2.8) owing to the extended domain of fluid flow, and thus increases P_b . Apparently, increasing η results in an increase of the total viscous retardation of the bubble, which necessitates an increase of P_b in order to maintain the same bubble speed (Ca).

The influence of Γ

Figures 10–12 demonstrate the influence of the wall elastance parameter, $\Gamma = KH^2/\gamma$ on the reopening system with Ca and η fixed. This is equivalent to investigating the effect of elastance on the system by modification of the elastic constant K , or modification of the stress-free location of the wall, H . Increasing H causes an increase in the depth of the thin film surrounding the bubble, which may influence shear stresses. Figure 10(a) shows that variation of Γ causes a large change in P_b . Increasing Γ by increasing K results in a stiffer system, and causes the dimensionless (and dimensional) bubble pressure to rise in order to preserve the same Ca . This behaviour is partially due to the reduction of the channel width, L , with increasing Γ , and hence a reduction of the area over which pressure is applied (figure 11). Furthermore, with increasing Γ , the range over which significant shear stress exists is extended (figure 12b), increasing bubble viscous retardation. In order to compensate for each of these effects, P_b must increase, as described by (2.8). This result, in conjunction with figure 10(a), indicates that airways with smaller upstream widths require higher pressures to open, a behaviour agreeing with measurements made by Gaver *et al.* (1990).

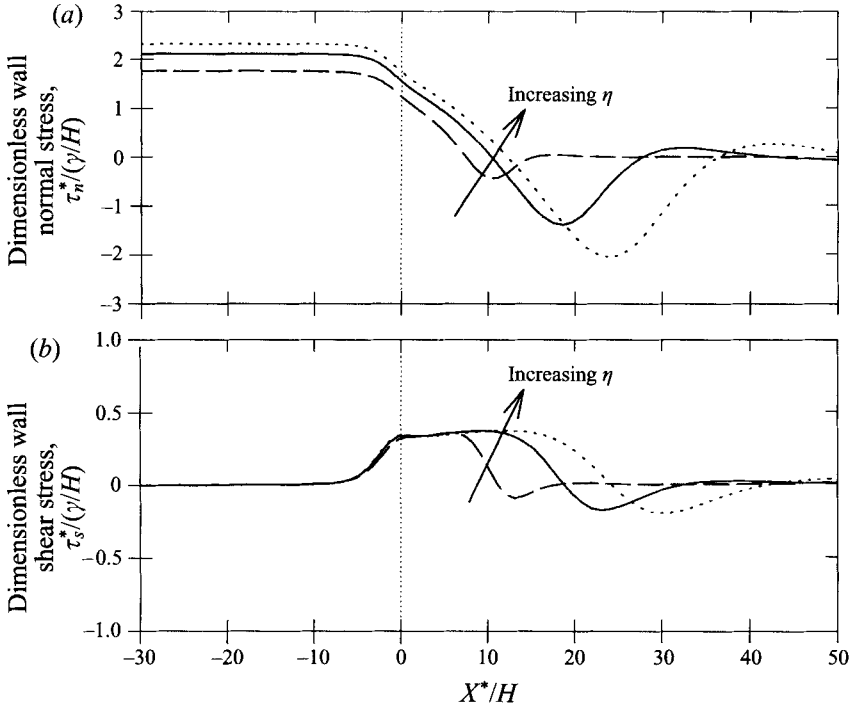


FIGURE 9. The influence of $\eta = T/\gamma$ on wall stresses. $\Gamma = KH^2/\gamma = 0.5$, $Ca = \mu U/\gamma = 0.5$. ----, $\eta = 10$; —, $\eta = 100$; ·····, $\eta = 250$. (a) Dimensionless normal stress, $\tau_n^*/(\gamma/H)$; (b) dimensionless shear stress, $\tau_s^*/(\gamma/H)$.

The effect of increasing H can also be deduced from figure 10(a). At large Γ , P_b increases linearly with Γ , indicating that P_b^* increases linearly with H . This increase is due to the fact that as Γ increases, the wall flattens and the system behaves more like that of a semi-infinite bubble progressing through a rigid channel. In this limit, the bubble-width to channel-width ratio ($\beta = 1 - H/L^*$) approaches a value that is dependent only upon Ca . For $Ca = 0.5$, the rigid channel result is indicated in figure 10(d). In order for the flexible-walled system to approach this result, the walls must separate further, necessitating an increase in P_b . So, in the regime where the flexible-walled system behaves as a rigid-walled channel, the linear wall equation used in this study results in the linear relationship between P_b^* and H seen in figure 10(a). Below, §6.1, we re-analyse these data to determine whether the capillary pressure scale is better represented by γ/L^* , as indicated by experiments.

Figures 10(b) and 10(c) show the influence of Γ on R_{tip} and ΔP , respectively. Increasing Γ causes the tip to become slightly more pointed, owing to squeezing of the walls. This results in a modest increase of ΔP . This behaviour may compensate for the increased shear stress in the system as Γ increases.

Streamlines

Figures 13(a) and 13(b) demonstrate streamlines for $Ca = 0.2$ and $Ca = 0.5$ with $\Gamma = 0.5$ and $\eta = 100$. The most significant difference between the streamline patterns is the existence of a recirculation region near the bubble tip at low Ca , which disappears at higher Ca . This behaviour is similar to that predicted by Coyle, Macosko & Scriven (1986) in their analysis of film-splitting flows between two counter-rotating rolls. The vortices within the recirculation region are isolated from the remainder of the fluid in

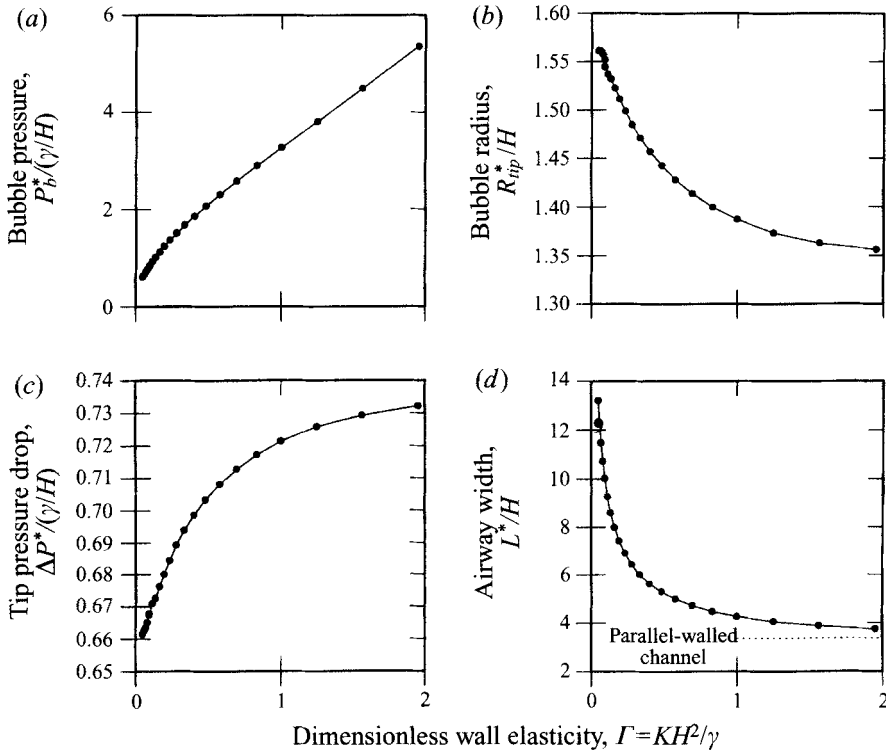


FIGURE 10. The influence of $\Gamma = KH^2/\gamma$ on the reopening behaviour. $\eta = T/\gamma = 100$, $Ca = \mu U/\gamma = 0.5$.

the channel by a closed stagnation streamline (shown with a dotted line). Low Ca flows in rigid channels exhibit similar recirculation regions; however, the vortices extend indefinitely (Reinelt & Saffman 1985), and thus are not isolated from the incoming fluid. For this reason, we speculate that surfactant transport in the flexible-walled system will differ fundamentally from that predicted in rigid channels (Ratulowski & Chang 1990).

The disappearance of the recirculation region with increasing Ca is similar to that seen in parallel channel flows. The lack of recirculation is not a feature that is indicative of the right-hand branch – lower Ca flows in more compliant systems (lower Γ) exhibit recirculation similar to figure 13(a) while on the right-hand branch. Note that in figures 13(a) and 13(b) retrograde motion in the laboratory frame is not demonstrated owing to the translation to the bubble-tip frame of reference. In the laboratory frame, retrograde flow exists near the necking location of the wall.

5. Multiple branch behaviour of P_b – Ca relationship

The results shown above demonstrate several interesting features of this system. The most fascinating behaviour is the non-monotonic relationship between P_b and Ca , which indicates that a given P_b can be associated with two distinct values of Ca . Below, we examine the influence of Γ and η on this behaviour. To explain the physics of each branch, we next examine the limiting cases appropriate for each branch, and derive scaling relationships for different regimes in the domain. These scalings are useful in understanding the dominant force balances, and identify the physical differences

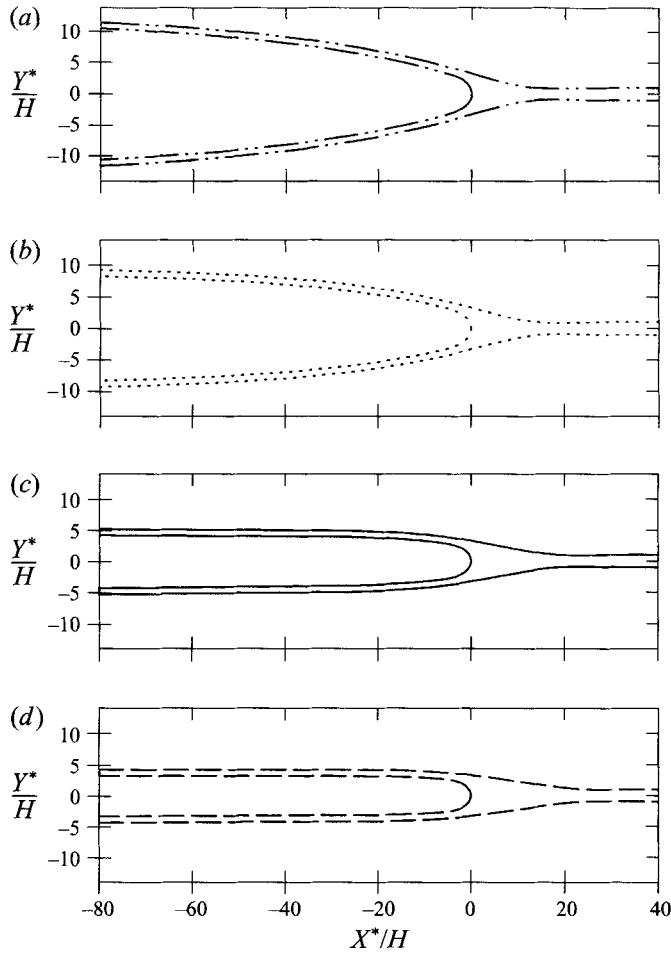


FIGURE 11. The influence of $\Gamma = KH^2/\gamma$ on the domain. $\eta = T/\gamma = 100$, $Ca = \mu U/\gamma = 0.5$.
 (a) $\Gamma = 0.05$. (b) $\Gamma = 0.1$. (c) $\Gamma = 0.5$. (d) $\Gamma = 1.0$.

between the left-hand and right-hand branches. Following the analysis, we demonstrate the transition from one branch to another, and show that this behaviour is consistent with the derived relationships.

5.1. The influence of Γ and η on the relationship between P_b and Ca

Figures 14(a) and 14(b) demonstrate the influence of wall elastance and tension on the pressure/velocity behaviour of the system. These figures show both lubrication and boundary-element results, and show that in some cases these predictions coincide for $Ca = O(1)$. Figure 14(a) shows that the non-monotonic relationship between P_b and Ca exists over a wide range of Γ . The turnaround from the left-hand to right-hand branches occurs at smaller Ca when Γ is reduced. This suggests that increased wall deflection (see figure 11) is responsible for the onset of the right-hand branch of the P_b – Ca relationship. Figure 14(b) shows that increasing η does not influence small Ca behaviour, but does reduce the Ca associated with a turnaround from the left-hand to the right-hand branches. This result implies that an extended transition from the fully open to fully closed portion of the channel might be responsible for the conversion from the left-hand to right-hand branches, as will be shown in §5.3. Together, figures 14(a) and 14(b) indicate that the downstream suction pressure, created by the product

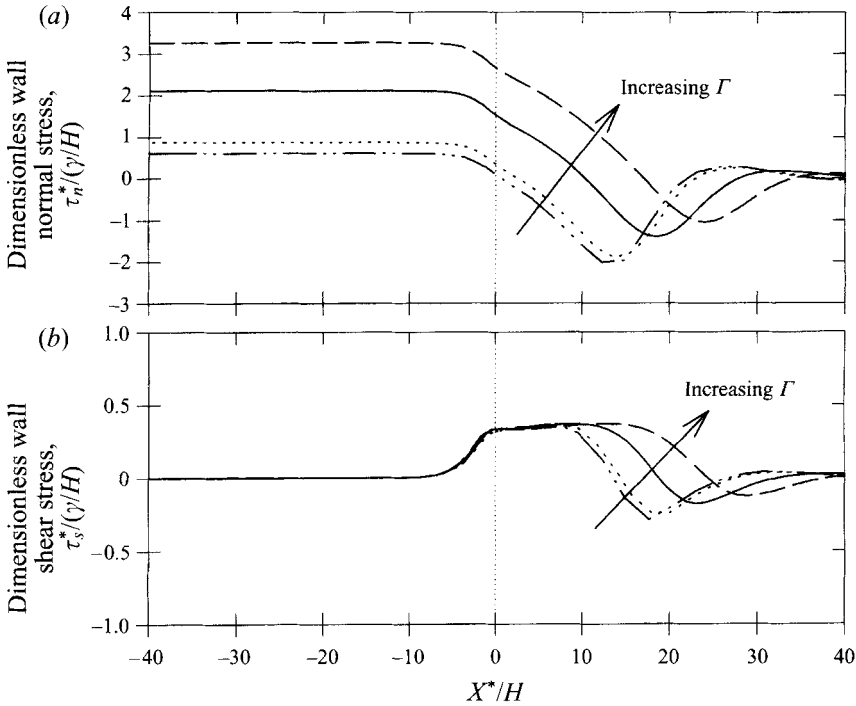


FIGURE 12. The influence of $\Gamma = KH^2/\gamma$ on wall stresses. $\eta = T/\gamma = 100$, $Ca = \mu U/\gamma = 0.5$. $\dashdot\text{---}$, $\Gamma = 0.05$; $\cdots\cdots$, $\Gamma = 0.1$; --- , $\Gamma = 0.5$; --- , $\Gamma = 1.0$. (a) Dimensionless normal stress, $\tau_n^*/(\gamma/H)$; (b) dimensionless shear stress, $\tau_s^*/(\gamma/H)$.

of wall curvature and tension (equation (2.4)), may also contribute to turnaround. However, this does not appear to be due to the suction's influence on the downstream pressure gradient, as the pressure gradient (demonstrated approximately by figures 6(a), 9(a) and 12(a)) is almost entirely a function of Ca . Comparing the lubrication theory to boundary-element results in figures 14(a) and 14(b) indicates that lubrication theory can accurately determine P_b when $Ca \sim O(1)$ if Γ is small. This good correlation can be understood by the scaling behaviour described below.

5.2. Scaling relationships

It is possible to identify asymptotic structures of the solutions within suitable ranges of the governing parameters. These scaling relationships are instrumental in understanding the left-hand and right-hand branches of the P_b - Ca relationship. We consider the limits $Ca = \mu U/\gamma \ll 1$, in which case surface tension forces are expected to dominate viscous forces, and $Ca/\eta = \mu U/T \ll 1$, where wall tension forces dominate viscous forces. Since both limits are singular, it is likely that short transitional regions of rapid variation will exist in which surface (or wall) tension and viscous forces will be in balance.

In this analysis, it is important to identify conditions in which the wall location is determined primary by either wall tension or by elasticity, since this helps determine the Ca ranges for the behaviour of interest. To do so, consider the flow ahead of the bubble where $h = O(1)$. As described above, computations in this region show that the pressure gradient is largely independent of η and Γ , as can be seen in figures 9(a) and 12(a). This pressure gradient is determined predominantly by viscous stresses, which from (3.5) are of $O(Ca)$. From the linearized wall equation (3.3), the lengthscale over

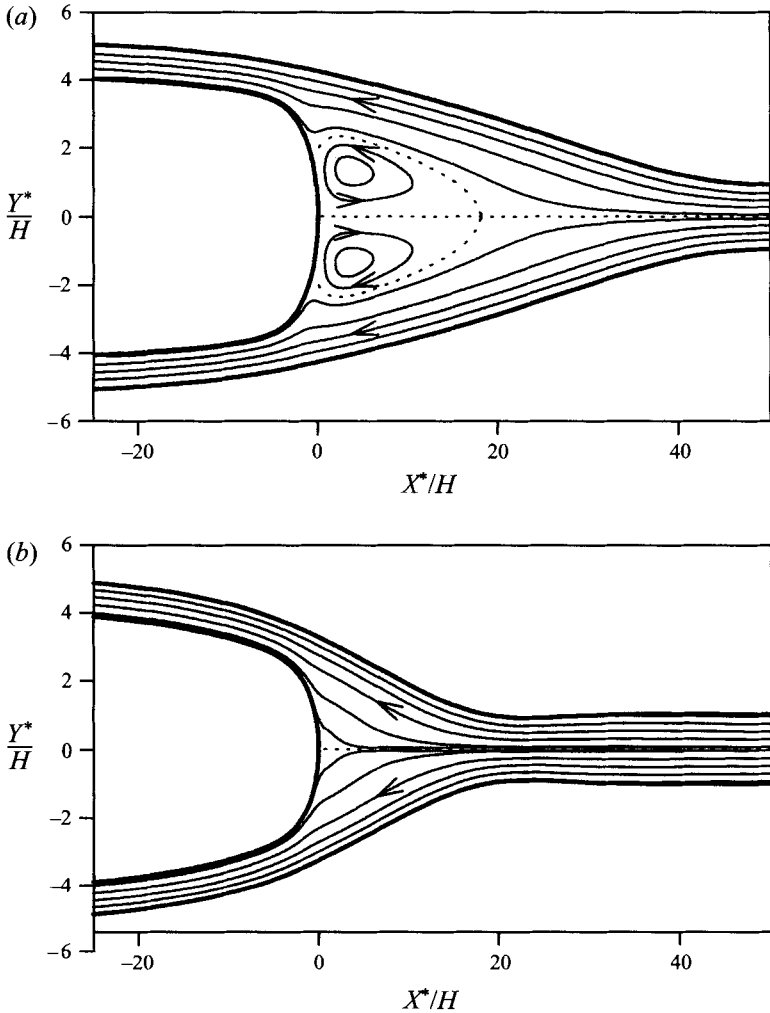


FIGURE 13. The influence of $Ca = \mu U/\gamma$ on streamlines. $\Gamma = KH^2/\gamma = 0.5$, $\eta = T/\gamma = 100$.
 (a) $Ca = 0.2$, (b) $Ca = 0.5$.

which elastic forces operate is $X_{el} = O(\Gamma/Ca)$. Likewise, the lengthscale for wall tension forces is $X_{ten} = O((\eta/Ca)^{1/3})$. These two lengthscales are comparable when $Ca = O(Ca_s)$, where $Ca_s = (\Gamma^3/\eta)^{1/2}$. When $Ca \ll Ca_s$, $X_{el} \gg X_{ten}$ and we anticipate that the wall response ahead of the bubble will be dominated by elastic forces. In contrast, when $Ca \gg Ca_s$, $X_{ten} \gg X_{el}$, and the dominant wall force ahead of the bubble is due to longitudinal tension. Below, we consider separately very small and very large values of Ca to understand the left-hand and right-hand branch behaviour. These limits are: (i) $Ca \ll \min(1, Ca_s)$, where surface tension dominates viscous forces and elastic forces control the downstream wall response where $h = O(1)$, and (ii) $\max(1, Ca_s) \ll Ca \ll \eta$, where viscous forces dominate surface tension forces and wall tension controls the downstream response. These limiting cases describe the physics of the left-hand and right-hand branches of the P_b - Ca relationship, respectively, and are discussed below.

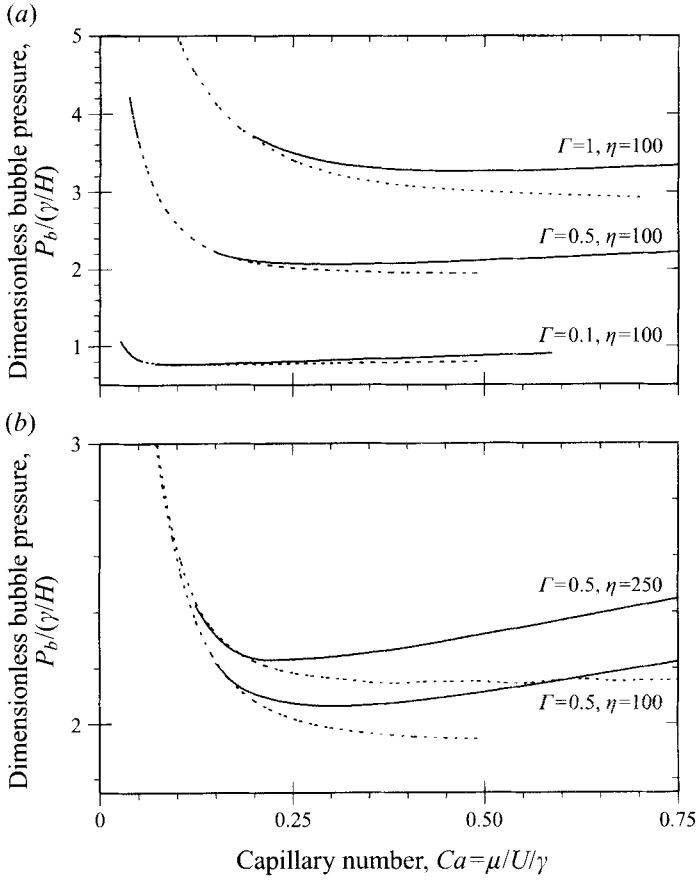


FIGURE 14. The influence of Γ and η on P_b - Ca relationship. (a) The influence of Γ , $\eta = 100$; (b) the influence of η , $\Gamma = 0.5$. $\cdots\cdots$, lubrication theory; —, boundary-element method.

5.2.1. Left-branch behaviour ($Ca \ll \min(1, Ca_s)$)

The domain for the small Ca parameter range is shown in figure 15(a), which is divided into 5 specific regimes of interest. Below, we derive the scales for each of these regions, and then use this information with (2.8) to identify the region that dominates the resistance to reopening, and thus sets the characteristics of the left-hand branch.

Regimes

Far upstream of the tip, a ‘uniform bubble’ regime exists where the bubble has nearly parallel sides, the fluid has a thickness $h-f \sim 1$, and $P = P_b$. At the bubble tip, surface tension stresses dominate viscous stresses, and, using the terminology of Park & Homsy (1984), a ‘capillary–statics’ region is anticipated to exist where pressure is nearly constant. So, the interface at the bubble tip is approximately semi-circular with a radius R , and the fluid pressure directly outside of the bubble tip is $P \sim P_b - 1/R$.

Between the ‘uniform bubble’ and ‘capillary–statics’ regimes, a ‘capillary–viscous’ transition region exists. Here, the pressure drop of $\Delta P = O(1/R)$ exists over a lengthscale X_{C-V} , say. This pressure drop occurs owing to a balance of surface tension and viscous forces. From (3.5), the viscous pressure gradient for a film thickness of $O(1)$ is of $O(Ca)$. So, the pressure drop across this region is $\Delta P = O(Ca X_{C-V}) = O(1/R)$. Since from (3.2) $\Delta P = O(1/X_{C-V}^2)$, then $X_{C-V} = O(Ca^{-1/3})$, and $\Delta P = O(Ca^{2/3})$.

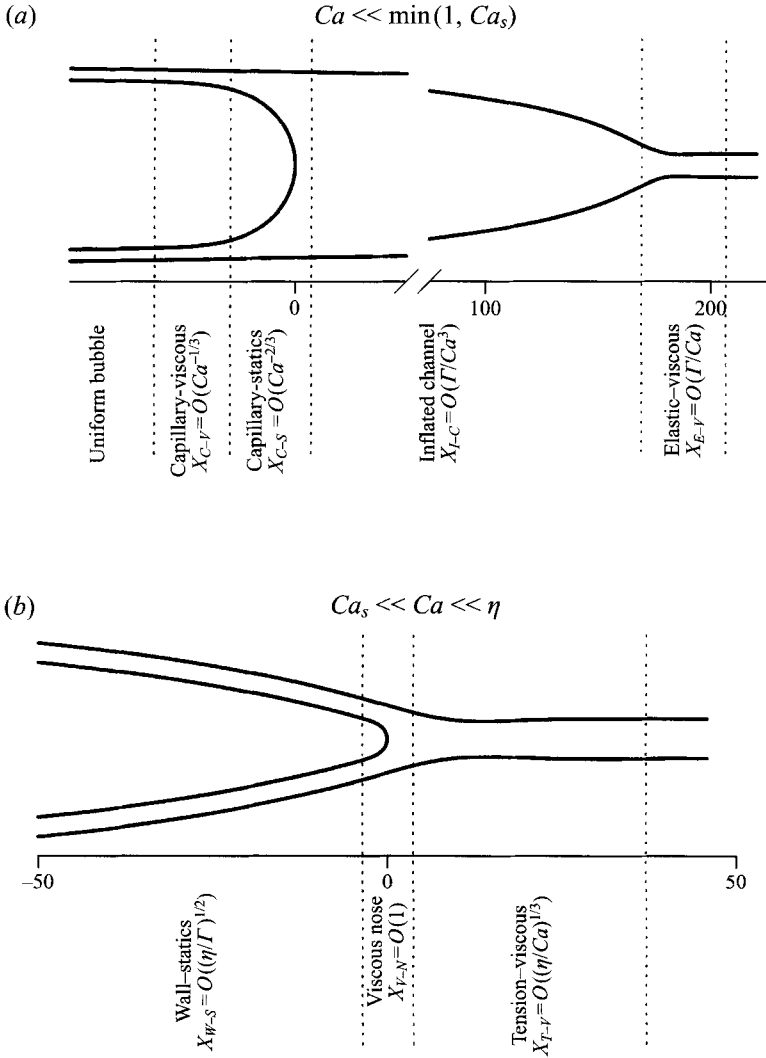


FIGURE 15. Scaling relationships. (a) Surface tension/wall elasticity dominated domain, $Ca \ll \min(1, Ca_s)$; (b) viscosity/wall tension dominated domain, $\max(1, Ca_s) \ll Ca \ll \eta$.

This pressure drop is identical to that identified by Bretherton (1961) and Park & Homsy (1984) in lubrication analyses of semi-infinite bubbles progressing through parallel-walled rigid channels, and will be discussed below in §5.4. From this result, the tip radius of curvature is $R_{tip} = O(Ca^{-2/3})$. Since the film thickness is only $O(1)$, the channel width $L = O(R) = O(Ca^{-2/3})$. This result provides an estimate of the bubble pressure,

$$P_b = O(\Gamma Ca^{-2/3}) \quad Ca \ll \min(1, Ca_s), \tag{5.1}$$

which decreases with increasing Ca .

Directly downstream of the bubble tip an ‘inflated channel’ regime exists where the pressure inflates the elastic tube so that $h = O(L) \gg 1$. From lubrication theory using (3.5) with $f = 0$, $\partial p / \partial x = O(Ca/L^2) = O(Ca^{7/3})$. The pressure in this regime decays from $O(P_b)$ to zero over the length X_{I-C} , indicating from (5.1) that $X_{I-C} = O(\Gamma Ca^{-3})$, which is an extremely long region. Finally, this region attaches downstream to an

‘elastic–viscous’ region where $h = O(1)$. Since $Ca \ll Ca_s$, this region has a lengthscale $X_{E-V} = O(X_{el}) = O(\Gamma/Ca)$.

Resistance to reopening

The macroscopic momentum balance given by (2.8) describes the balance between the applied pressure and the resistance to reopening provided by τ_x . Examining each regime’s contribution to the resistance provides one explanation of the left-hand branch behaviour.

Separating the

$$\int_{-\infty}^{\infty} (\tau_x)_{wall} ds$$

sequentially into components (left to right) based upon each of the 5 regimes described above and shown in figure 15(a),

$$P_b = O\left(\begin{array}{c} \text{Uniform} \\ \text{bubble} \end{array} \left[0 + (Ca)(Ca^{-1/3}) + \left(\begin{array}{c} \text{Capillary-} \\ \text{statics} \end{array} \right) (Ca^{-2/3}) + \left(\begin{array}{c} \text{Inflated-} \\ \text{channel} \end{array} \right) \left(\frac{\Gamma}{Ca^3} \right) + \left(\begin{array}{c} \text{Elastic} \\ \text{viscous} \end{array} \right) \left(\frac{\Gamma}{Ca} \right) + 1 \right] \right)$$

$$= O\left(\frac{\Gamma}{Ca^{2/3}} \right). \quad (5.2)$$

Each non-zero term representing the $\int \tau_x ds$ is separated into two components: the first is a measure of the local $|\tau_x|$ for each region, and the second reflects the length of that region. In these approximations, $|\tau_x| \sim Ca/(\text{local gap width})$. The final result is identical to the asymptotic result derived above (5.1). This calculation shows that P_b must primarily overcome $\int \tau_x ds$ over the ‘inflated channel’ region. This result shows that the reduction of P_b with increasing Ca results from the shortening of the ‘inflated channel’ region, which reduces the $\int \tau_x ds$ even though $|\tau_x|$ increases with Ca . This behaviour will be demonstrated in more detail in §5.3 with respect to the transition from the left-hand to the right-hand branches.

A curious result of the analysis above is that the maximum local driving force ($\partial p/\partial x$) occurs in the ‘capillary–viscous’ regime, while the global retarding force is dominant in the ‘inflated channel’ region. Lubrication theory is capable of accurately predicting the behaviour at low Ca because the small slope approximations are accurate in both of these regions.

5.2.2. Right branch behaviour ($\max(1, Ca_s) \ll Ca \ll \eta$)

The large- Ca asymptotic structure can be expected to exist for large values of η , and is broken into 3 distinct regions, as shown in figure 15(b). Below we derive the scales for each of these regions and, as above, use this information with (2.8) to identify the region that dominates the resistance to reopening, and thus sets the characteristics of the right branch.

Regimes

For $\max(1, Ca_s) \ll Ca$, viscous forces dominate surface tension forces, and wall tension dominates elasticity when the film thickness is $O(1)$. If $Ca \ll \eta$, wall tension forces dominate viscous forces. Upstream of the bubble the fluid is static with respect to the channel wall, and when both constraints are satisfied, a ‘wall–statics’ region will dominate region I, where $P = P_b$ uniformly. Far upstream the bubble inflates to a maximum width of $O(P_b/\Gamma)$, and elastic and tension forces balance to contribute to the wall and bubble shape. From (3.3), this region has a length $X_{W-S} = O((\eta/\Gamma)^{1/2})$. Note

that the wall in this regime is canted at a small angle over an extended length, a characteristic that is important in the calculation of τ_x used below.

Directly downstream of the ‘wall–statics’ regime, viscous forces dominate surface tension forces near the bubble tip in the ‘viscous nose’ region. Assuming that $h = O(1)$ in the neighbourhood of the tip, and that viscous normal stresses operate over a longitudinal lengthscale of $X_{V-N} = O(1)$, the tip radius of curvature is $O(1)$, and the pressure drop across this region is thus $O(Ca)$. Evidence in support of the ‘viscous nose’ region is given by figures 4(b) and 4(c) which show that the tip pressure jump decouples from the bubble-tip radius of curvature at high Ca .

Downstream of the bubble tip, $h = O(1)$, and a ‘tension–viscous’ region exists where the pressure drop occurs across a lengthscale $X_{T-V} = X_{ten} = O((\eta/Ca)^{1/3})$. From (3.5) the viscous pressure gradient is $O(Ca)$, so that the total pressure drop is $O(Ca X_{T-V}) = O(\eta^{1/3} Ca^{2/3})$. Since $Ca \ll \eta$, this contribution to the total pressure drop far exceeds that due to viscous stresses at the nose. Therefore, the bubble pressure in this limit is:

$$P_b = O(\eta^{1/3} Ca^{2/3}) \quad \max(1, Ca_s) \ll Ca \ll \eta \quad (5.3)$$

which increases with Ca , and in dimensional form is independent of the surface tension.

Resistance to reopening

From the scaling relationships derived above, it is evident that the right-hand branch behaviour is dominated by a balance between viscous fluid forces and wall tension, and that P_b given by (5.3) is independent of Γ . While the Γ -independence is not observed in figure 14(a), this may be due to the fact that simulations did not extend to high enough values of Ca or η to exhibit this behaviour. From the data presented in figure 14(a), however, it is apparent that the slope of the right-hand branch is largely independent of Γ , so at large Ca the relative deviation between P_b with different Γ will be small.

From the scaling analysis, it is clear that the major component of the pressure drop in the system occurs in the ‘tension–viscous’ regime downstream of the meniscus, which increases in length with Ca . However, an alternative explanation to the right-hand branch behaviour arises by examining the control-volume momentum equation (2.8). Separating the

$$\int_{-\infty}^{\infty} (\tau_x)_{wall} ds$$

sequentially into components (left to right) based upon each of the 3 regimes shown in figure 15(b),

$$\begin{aligned} P_b &= O\left(\frac{\Gamma}{\eta^{1/3} Ca^{2/3}} \left[\left(\frac{\eta^{1/6} Ca^{4/3}}{\Gamma^{1/2}}\right) \left(\frac{\eta}{\Gamma}\right)^{1/2} + (Ca)(1) + (Ca)\left(\frac{\eta}{Ca}\right)^{1/3} + 1 \right]\right) \\ &= O(\eta^{1/3} Ca^{2/3}), \end{aligned} \quad (5.4)$$

which is consistent with the scaling analysis above (5.3). As above, each term representing the $\int \tau_x dx$ is separated into two components: the first is a measure of the local $|\tau_x|$ for each region, and the second reflects the length of the region. For the ‘wall–statics’ region $|\tau_x| \sim P_b n_x \sim (P_b)(L/X_{W-S}) \sim \eta^{1/6} Ca^{4/3}/\Gamma^{1/2}$. This analysis shows the interesting result that the dominant term arises from the x -component of the normal stress (P_b) in the ‘wall–statics’ region. So, although the majority of the pressure drop is distributed over the ‘tension–viscous’ regime, this drop is reflected in the x -component of the momentum balance in the wall–statics region.

The analysis of large- Ca reopening shows that the dominant regions are the ‘wall–statics’ and ‘tension–viscous’ regimes. Both regions are characterized well by small slope approximations, and thus their behaviour can be captured by lubrication theory. This correlation is shown in figure 14(a) for $\Gamma = 0.1$ ($Ca_s \approx 10^{-3}$). So, apparently, when $\Gamma \ll 1$, lubrication theory is capable of describing the leading-order right-hand branch behaviour even through $Ca \sim O(1)$.

5.3. Transition from the left-hand to right-hand branches

As shown above, the contribution of $\int \tau_x ds$ to P_b shifts from the ‘inflated channel’ region downstream of the bubble tip in the left-hand branch to the ‘wall–statics’ region in the right-hand branch. In order to understand how Γ and η influence the transition behaviour, it is useful to explore the contributions of the upstream and downstream τ_x following (2.8). From the low- Ca scaling analysis, it is evident that the left-hand branch results in a decrease in P_b with increasing Ca owing to the extreme reduction in the length of the ‘inflated-channel’ regime. We approximate the length of this regime in the computational domain as the distance (\mathcal{L}) from the bubble tip to the x -location where $h = 1$. Figures 16(a)–16(c) show \mathcal{L} , the average downstream $\tau_x(|\tau_x|)$, and $\int \tau_x ds$ over this region for small η ($\eta = 2$, $\Gamma = 0.5$), where turnaround is not prevalent. In contrast, larger η ($\eta = 100$, $\Gamma = 0.5$) and decreased Γ ($\eta = 100$, $\Gamma = 0.05$) moderates the rate of decrease of \mathcal{L} (figure 16a). In addition, $|\tau_x|_{down}$, decreases with increasing η and is greatly reduced by decreasing Γ (figure 16b). In combination, these responses cause

$$\int_0^{\mathcal{L}} (\tau_x)_{wall} ds$$

to increase with increasing η or Γ . More importantly, though, is that fact that the rate of decrease of

$$\int_0^{\mathcal{L}} (\tau_x)_{wall} ds$$

with increasing Ca is greatly reduced for large Ca when η increases or Γ decreases. In fact, at large Ca when Γ is small or η is large, this contribution begins to slightly increase with increasing Ca , which is in sharp contrast with the behaviour observed for small η . This response indicates that wall tension lengthens \mathcal{L} , and reduces the rate of decrease in \mathcal{L} with increasing Ca , and thus is partially responsible for the onset of the right-hand branch of the P_b – Ca relationship. Perhaps the downstream wall suction prevents the decrease in \mathcal{L} , resulting in this behaviour. However, this response alone does not completely describe the transition to the right-hand branch.

To understand fully the transition behaviour, it is essential to examine the upstream contribution of τ_x . Figure 16(d) shows the contribution to P_b from the

$$\int_{-\infty}^0 (\tau_x)_{wall} ds.$$

This figure shows that the upstream contribution of τ_x increases with increasing Ca when η is large or Γ is small. This results from the ‘wall statics’ region upstream of the bubble tip being held at an angle (figures 8, 11, 15b), which causes the x -component of the normal stress ($\sim P_b$) to provide a significant contribution to τ_x over an extended distance. Increasing Ca extends the distance over which the wall is at an angle (figure 5), and thus increases the magnitude of

$$\int_{-\infty}^0 (\tau_x)_{wall} ds.$$

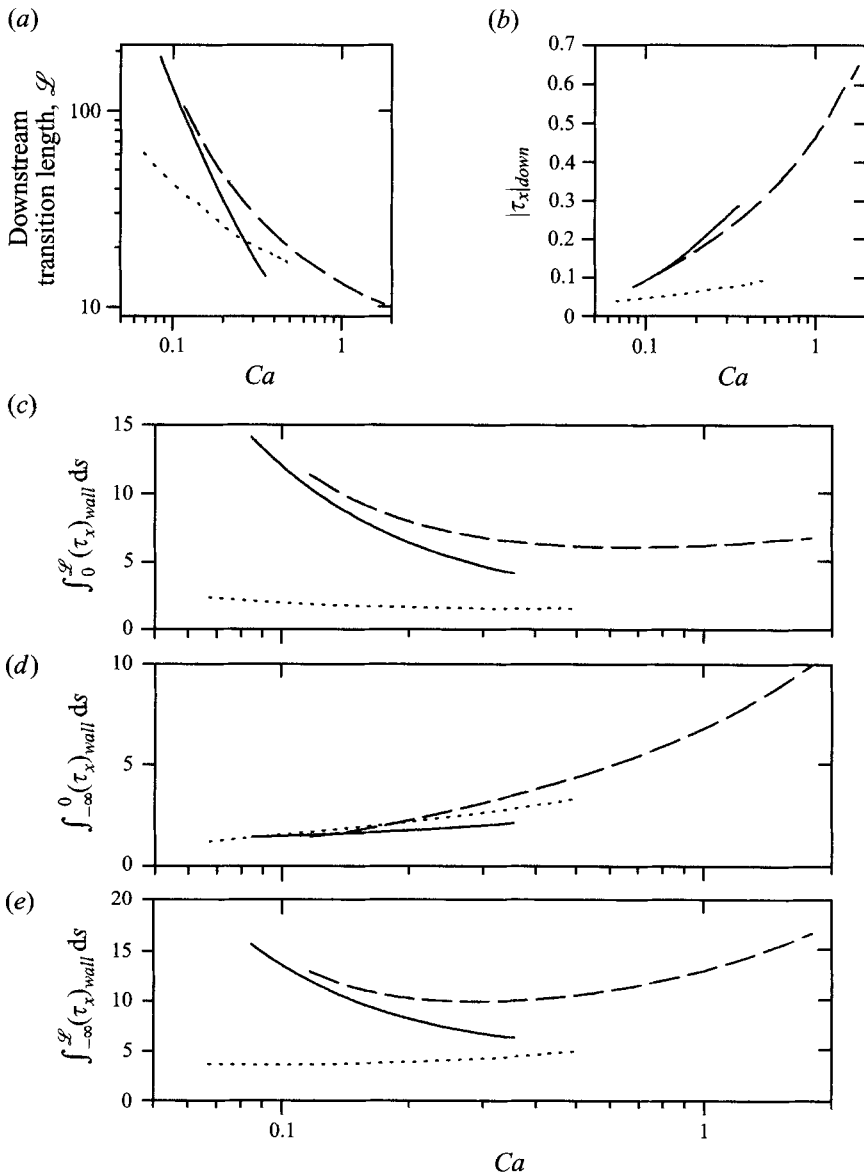


FIGURE 16. The influence of $\Gamma = KH^2/\gamma$, $\eta = T/\gamma$ on effect of τ_x on P_b . —, $\Gamma = 0.5$, $\eta = 2$; ----, $\Gamma = 0.5$, $\eta = 100$; ·····, $\Gamma = 0.05$, $\eta = 100$. (a) Downstream transition length, \mathcal{L} ; (b) average downstream x -component of stress $|\tau_x|$; (c) downstream contribution of τ_x to P_b ; (d) upstream contribution of τ_x to P_b ; (e) total contribution of τ_x to P_b .

For large η or small Γ , this behaviour begins to dominate the reduction of

$$\int_0^{\mathcal{L}} (\tau_x)_{wall} ds$$

with increasing Ca , and results in the transition from the right-hand to the left-hand branches of the P_b vs. Ca relationship, as shown in figure 16(e).

In summary, we have shown that the left-hand branch of the P_b – Ca relationship is dominated by the coupling of surface tension and elastic stresses. P_b decreases with

increasing Ca owing to a reduction in downstream resistance in the ‘inflated channel’ region that is caused by a decrease in the $\int \tau_x ds$ owing to the shortening of the regime with increasing Ca . The right-hand branch is dominated by an interaction of viscous and wall tension forces. The pressure drop occurs largely in the downstream ‘tension–viscous’ region, but is dominated in the macroscopic momentum balance by the ‘wall–statics’ contribution. Increasing η or decreasing Γ shifts the dominant contribution of the $\int \tau_x ds$ from downstream to upstream by tilting the upstream portion of the wall, inducing a large component of $\int \tau_x ds$ from the x -component of the normal stress upstream of the bubble, and causing P_b to increase with increasing Ca .

5.4. Comparison of left-branch to parallel-walled channel behaviour

The scaling relationships for $Ca \ll \min(1, Ca_s)$ in §5.2.1 provide information that is useful for further understanding the left-hand behaviour of the P_b – Ca relationship. In particular, the interfacial pressure drop in the ‘capillary–viscous’ region, ΔP , is of the same form as the Bretherton approximation (1961), implying that in this limit the system behaves as a parallel-walled channel. In addition, the scaling results show that wall tension does not determine the bubble pressure, a result that is consistent with the observations reported in figure 14(b). The behaviour in this regime is thus dominated by surface tension and wall elastic responses.

To determine whether the left-hand branch response is consistent with parallel-walled channel behaviour, we improve the approximation of P_b by considering the limit of $Ca \rightarrow 0$ for the singular case of $\eta = 0$ using lubrication theory. In the limiting case of $Ca \ll 1$, numerical solutions of the system of equations (3.9) indicate that the wall is approximately uniform, $h \rightarrow h_0$, and that the air–liquid interface has constant curvature, $f'' \rightarrow -\kappa$.

To evaluate κ , we investigate the bubble-tip regions I and II (the upstream and downstream regions) with constant interfacial curvature and channel width. Equation (3.6) gives as $\bar{x} \rightarrow -\infty$:

$$\left. \begin{aligned} h &\sim h_0 + \frac{4\lambda}{3\kappa^2 \bar{x}^3} + \dots, \\ f &\sim -\frac{\kappa}{2} \bar{x}^2 + A\bar{x} + B + \frac{2}{3\kappa^2 \bar{x}} + \dots, \end{aligned} \right\} \quad (5.5)$$

where A and B are arbitrary constants, h_0 is the wall displacement at the bubble tip, $\lambda = (3Ca)^{(2/3)}/\Gamma$, and $\bar{x} = (3Ca)^{1/3}x$. The dependence of h and f on L can be clarified by recognizing that $\tilde{h} = h - L$ and $\tilde{f} = f - (L - 1)$ removes L from (3.6). The solution of \tilde{h} and \tilde{f} depends only on λ . Note that since system (3.6) is autonomous, there exists a unique solution independent of the amplitude of the linearized solution used as an initial condition. From these solutions we obtain $\kappa \approx 0.64$.

Equation (3.6b) implies that $L - h_0 \sim \kappa\lambda$. Therefore, the pressure difference across the bubble tip is independent of Γ since, using the linear wall equation model,

$$\Delta P = (L - h_0) \Gamma \sim \kappa\lambda\Gamma \sim \kappa(3Ca)^{2/3} \quad \text{as } Ca \rightarrow 0. \quad (5.6)$$

which is consistent with the scaling analysis above. This suggests that at low Ca the bubble speed can be determined by the relationship between tip curvature and ΔP in the $\eta = 0$ case, and that downstream suction does not determine the bubble velocity. In addition, at low Ca the bubble tip is a semicircular cap that spans the void between the fluid covered channel walls, so $\Delta P \sim 1/(L - 1) \sim 1/L$. Substituting into (5.6),

$$L \sim \frac{1}{\kappa\Gamma\lambda} \sim \frac{1}{\kappa}(3Ca)^{-2/3} \quad \text{as } Ca \rightarrow 0. \quad (5.7)$$

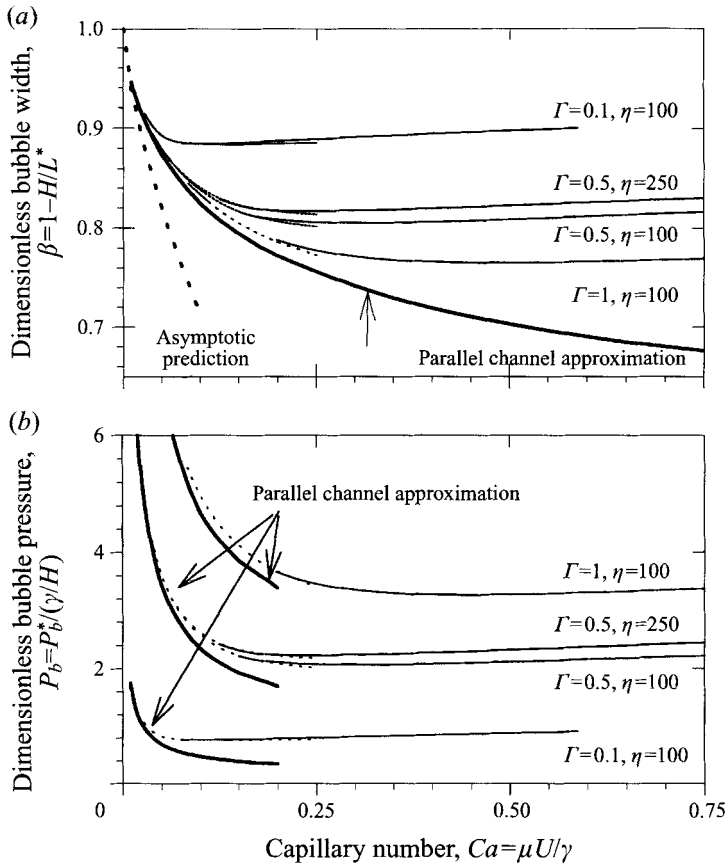


FIGURE 17. Comparison of flexible-walled system with parallel channel behaviour. (a) Dimensionless bubble width; (b) dimensionless bubble pressure.

From this result, the ratio of bubble width to channel width, $\beta = 1 - 1/L$, is given by

$$\beta = 1 - 1.33Ca^{2/3} \quad \text{as } Ca \rightarrow 0. \quad (5.8)$$

This power law relationship is identical to that found by the asymptotic analysis of two-phase flow in a rigid channel (Bretherton 1961; Park & Homsy 1984). Figure 17(a) demonstrates this relationship and compares the asymptotic result from (5.8) and the parallel-walled channel results determined by the boundary-element method (Halpern & Gaver 1994) with the flexible-channel predictions made by both lubrication theory and the boundary-element method. Clearly these parallel-wall channel results match the flexible-channel results for small to intermediate Ca . The range over which the approximation is accurate depends upon the wall tension and elastance. Increasing Γ and decreasing η extends the range over which the parallel-wall channel results provide good representations of the flexible-walled behaviour.

The good comparison between the parallel-wall predictions and the flexible-channel behaviour is due to the fact that at small Ca , the flexible-channel system is characterized by small wall slope and curvature (figure 5a). In this situation, the pressure decreases nearly linearly downstream of the bubble tip (figure 6a). The nearly constant $\partial P/\partial x$ and essentially parallel walls result in an approximately parabolic flow field, providing downstream flows in the neighbourhood of the bubble tip that are

similar to the end condition for two-phase flow in a rigid channel (Halpern & Gaver 1994). Unlike the rigid-channel problem, however, the flexible-walled case has predefined bubble film thickness, H , which must be satisfied by the macroscopic conservation of mass between the upstream and downstream ends of the channel. Nevertheless, at low Ca , the flexible-walled system responds so that the dimensionless bubble width, β , behaves in a manner very similar to that of the parallel-walled rigid channel, as demonstrated by figure 17(a).

This result provides another explanation for the left-hand branch of the P_b - Ca response. At low Ca , the flexible-walled structure behaves nearly as parallel-walled channel. The dimensionless bubble width responds as in the parallel-walled system, and thus at low Ca a reduction in Ca causes the bubble width ($\beta = 1 - H/L^* = 1 - 1/L$) to increase monotonically, with the limit of $\beta \rightarrow 1$ as $Ca \rightarrow 0$. Since the film thickness H is fixed, the upstream dimensional channel width L^* must increase with decreasing Ca . This can only occur by increasing the bubble pressure, P_b , to spread the channel walls (increase L), since $L = P_b/\Gamma + 1$. For this reason, a decrease in Ca leads to an increase of P_b , as seen in figure 14. This relationship is given by

$$P_b = \Gamma \left(\frac{1}{1-\beta} - 1 \right) \sim \frac{1}{\kappa\lambda} \sim \frac{\Gamma}{1.33} Ca^{-2/3} \quad \text{as } Ca \rightarrow 0, \quad (5.9)$$

which is consistent with the result from scaling arguments given above in (5.1).

Figure 17(b) shows the parallel channel approximation of the bubble pressure where $\beta = \beta_{\text{channel}}$ are data taken from the parallel-walled rigid-channel analysis published in Halpern & Gaver (1994). This figure shows that such an analysis is capable of predicting small Ca behaviour over a wide range of Γ . This derivation also explains the linear relationship between P_b and Γ shown in figure 10(a) for large Γ , where the walls are nearly parallel. Note, however, that this analysis cannot predict the onset of the right-hand branch of the P_b - Ca relationship, and does not discriminate between walls that have different values of η since, as we have shown above, the wall shape is determined by elasticity in this regime.

6. Discussion and conclusions

In this study, we have presented analysis of a semi-infinite bubble being forced through a compliant channel as an initial model of pulmonary airway reopening. In this section, we compare the results of this study to the general characteristics observed in benchtop and *in situ* experiments to show the relevance to the physiological behaviour. Finally, limitations of our analysis are discussed.

6.1. Pressure and shear stress scales

A significant aspect of the experimental analysis conducted by Gaver *et al.* (1990) related to the evaluation of the pressure scale for the reopening experiments. In that analysis, it was found that γ/R^* was an appropriate capillary scale for P_b^* , and collapsed the data from multiple experiments far better than the scale γ/H . In those studies, R^* was the upstream tube radius, which was an independent parameter of the study. In the analysis herein, the equivalent pressure scale would be γ/L^* , but is not an independent scale owing to the dependence on L^* on P_b^* , and thus was not chosen as the fundamental scale for the analysis. Instead, γ/H was chosen as the fundamental stress scale. Nevertheless, we can now use the results of our calculations to determine the physical scales for shear stress and P_b^* .

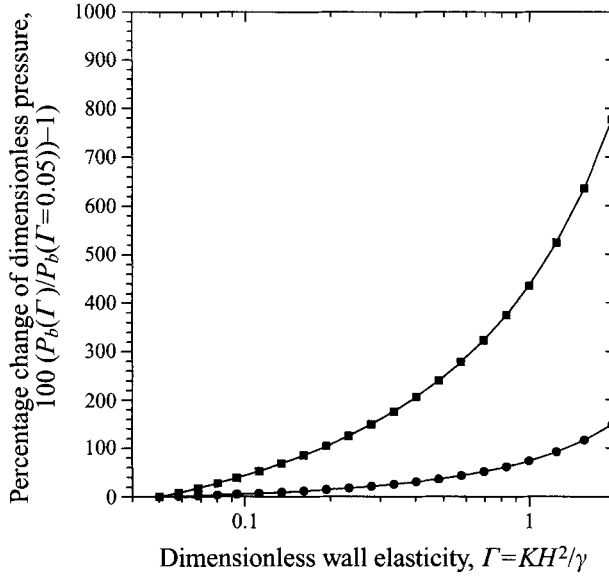


FIGURE 18. Pressure scale evaluation. Percentage change of ■, $P_b^*/(\gamma/H)$; ●, $P_b^*/(\gamma/L^*)$ as a function of Γ . $Ca = 0.5$, $\eta = 100$.

From the results given in figures 9(b) and 12(b), it is evident that γ/H is an appropriate scale for shear stress, since the extremum values of the wall shear stress are nearly independent of Γ and η . Therefore, it appears that the film thickness is instrumental in determining the shear stress in the system. In contrast, P_b^* does not appear to scale with γ/H , as can be seen in figure 10(a). In this figure, η and Ca are held constant, and Γ is varied. Increasing Γ decreases the wall compliance, reducing L for a given P_b . The significant increase in P_b with increasing Γ suggests that the physically appropriate pressure scale may be γ/L^* , which can be understood by the macroscopic analysis of §2.4. To check this hypothesis, we re-analysed the data of figure 10(a) using the pressure scales γ/H and γ/L^* and examined the percentage change in these dimensionless pressures arising from modification of wall elastance over the range $0.05 < \Gamma < 2$ with $Ca = 0.5$, and $\eta = 100$. The results of this analysis are given in figure 18, which shows that at low Γ , the percentage change in $P_b^*/(\gamma/L^*)$ is far smaller than that of $P_b^*/(\gamma/H)$, showing that P_b^* scales with γ/L^* . This scaling appears to become less valid when Γ increases, corresponding to activity along the left-hand branch. So, in summary, at small to moderate Ca on the right-hand branch, the bubble pressure in highly compliant systems scales approximately with γ/L^* , while wall shear stress scales with γ/H .

6.2. Yield pressures

Another significant result of the benchtop airway reopening studies was the identification of yield pressure phenomena. In these experiments, the yield pressure (P_{yield}^*) was taken to be the pressure corresponding to the zero- Ca limit of steady-state reopening. This pressure is thought to correspond to the pressure that must be exceeded in order to initiate reopening. Macklem (1971) originally proposed that such a pressure would exist, but thought that $P_{yield}^* \sim 2\gamma/R^*$, owing to the pressure drop across a hemispherical meniscus in a tube of radius R^* . In a rigid channel, this would correspond to a $P_{yield}^* \sim \gamma/L^*$. Experiments have not heretofore measured the true

start-up P_{yield}^* of these systems, but rather have reported an ‘apparent’ P_{yield}^* corresponding to the zero- Ca intercept of the steady-state reopening behaviour. Measurements by Gaver *et al.* (1990) showed an ‘apparent’ $P_{yield}^* \sim 8\gamma/R^*$, indicating that wall flexibility greatly decreased the bubble-tip radius of curvature. Naureckas *et al.* (1994) and Yap *et al.* (1994), used *in situ* models, and identified ‘apparent’ P_{yield}^* that were consistent with Gaver *et al.*’s measurements. However, recent measurements by Hsu *et al.* (1994) have shown ‘apparent’ P_{yield}^* as low as $3.1\gamma/R^*$. The smaller value of the ‘apparent’ P_{yield}^* was attributed to measurements being taken at smaller Ca than the original measurements by Gaver *et al.* (1990). All of the above-mentioned benchtop experiments were conducted in compliant tubes, with complex reopening geometries and nonlinear wall behaviour, where the upstream radius was R^* , but the tube buckled to a ribbon-like configuration at the bubble tip. For these reasons, these measurements of the ‘apparent’ P_{yield}^* cannot be compared directly to the two-dimensional approximations described herein. It is more appropriate to compare these predictions to the recent studies by Perun & Gaver (1995*a, b*), who analysed two-dimensional channel models. Perun & Gaver (1995*a*) studied channels with highly nonlinear wall support in which the walls were highly compliant ($\Gamma \ll 1$) when uninflated, but were rigidly restrained ($\Gamma \gg 1$) in the upstream inflated region owing to constraints imposed by two parallel rigid plates separated by a fixed distance, $2L^*$. These studies demonstrated an ‘apparent’ $P_{yield}^* \sim 1.85\gamma/L^*$. In channel experiments with nearly linear elastic support, which most closely resemble the models used in the analysis in this paper, Perun & Gaver (1995*b*) identified an ‘apparent’ P_{yield}^* of approximately 13 to $16.5\gamma/L^*$.

Unfortunately, owing to the left-hand branch behaviour, an ‘apparent’ P_{yield}^* from the analytical model cannot be approximated by the P_b corresponding to the zero- Ca intercept. Instead, a minimum of the P_b - Ca relationship exists that reflects the minimum pressure, P_{min} , in which a steady-state response is expected to exist. As shown in figure 14, P_{min} is a function of both Γ and η . At low Ca , the influence of η is minor, since the system is dominated by wall elasticity (§5.3), so P_{min} is most strongly influenced by Γ . The influence of Γ on P_{min}^* is partially identified by scaling P_{min}^* with γ/L^* , as discussed above. Figure 19(*a*) presents these data, and shows that $P_{min}^*/(\gamma/L^*)$ is further influenced by a decrease in Γ owing to the decrease in the Ca corresponding to P_{min} . This result shows $P_{min}^* \sim 6\gamma/L^*$ for $\Gamma = 0.05$; however, P_{min}^* may decrease further with increasing channel compliance (decreasing Γ). With decreasing Γ , this result may approximate the ‘apparent’ P_{yield}^* from experimental measurements using highly compliant channels. However, this is not the actual P_{yield}^* that would occur at system start-up.

To predict the true P_{yield}^* of the system, we define the yield pressure to be the largest bubble pressure for a static circular meniscus in the compliant channel. We assume that the wall is dry upstream of the bubble tip, with constant pressure, P_b . Downstream, the system is static, so $P = 0$. At yield, $P_b = P_{yield}^*$ and the bubble is circular with radius $1/P_{yield}^*$ and meets the wall tangentially. We define the contact line as existing at $x = x_c$, with the bubble tip centred at $x = 0$. Then, the equation for the meniscus shape is given by

$$f = \left(\frac{1}{P_{yield}^2} - x^2 \right)^{1/2}, \quad x_c \leq x \leq \frac{1}{P_{yield}}. \quad (6.1)$$

$$\left. \begin{aligned} h &= A e^{(\Gamma/\eta)^{1/2}x} + \frac{P_{yield}}{\Gamma} + 1, & x \leq x_c, \\ h &= B e^{-(\Gamma/\eta)^{1/2}x} + 1, & x \geq x_c. \end{aligned} \right\} \quad (6.2)$$

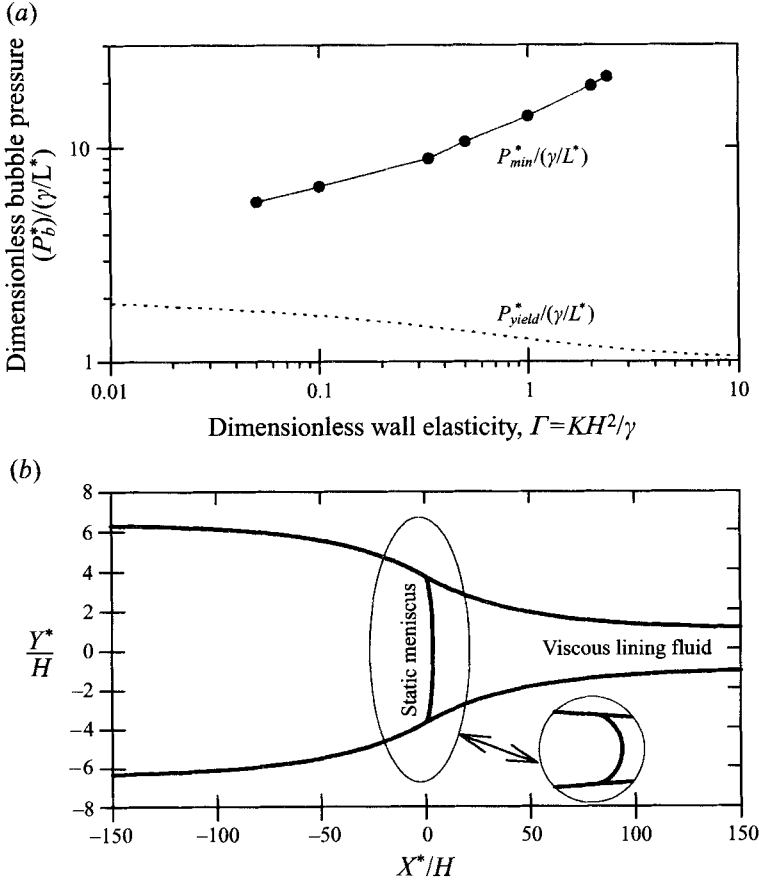


FIGURE 19. (a) Estimates of $P_{yield}^*/(\gamma/L^*)$ and $P_{min}^*/(\gamma/L^*)$ as a function of Γ . $\eta = 100$; (b) representative static meniscus profile at P_{yield}^* . $\Gamma = 0.005$, $\eta = 100$.

The wall shape is calculated using the lubrication approximation of the wall equation (3.3), resulting in A and B . x_c and P_{yield} are determined by satisfying continuity of position and slope of h at $x = x_c$, with the meniscus intersecting the wall tangentially, so $f = h, f_x = h_x$ at $x = x_c$. Comparison between numerical solutions of this system and asymptotic solutions based upon $(\Gamma/\eta)^{1/2}x_c \ll 1$ (small meniscus slope at x_c) show that the approximate solutions are accurate for $\eta \gg 1$, a condition that also assures that the lubrication approximations used in deriving (6.2) are valid. A representative profile of the steady-state system at yield is given by figure 19(b) for $\Gamma = 0.05$ and $\eta = 100$. This analysis shows that the results are insensitive to η to $\eta \gg 1$, and

$$\frac{P_{yield}^*}{\gamma/H} \sim -\Gamma + (\Gamma^2 + 2\Gamma)^{1/2}, \quad \text{or} \quad \frac{P_{yield}^*}{\gamma/L} \sim 2 + \Gamma - \Gamma \left(1 + \frac{2}{\Gamma}\right)^{1/2}. \quad (6.3)$$

The derived relationship (6.3b) is given in figure 19(a), and shows that $P_{yield}^*/(\gamma/L^*) < P_{min}^*/(\gamma/L^*)$. From (6.3b),

$$\lim_{\Gamma \rightarrow \infty} \left(\frac{P_{yield}^*}{\gamma/L^*} \right) = 1, \quad \lim_{\Gamma \rightarrow 0} \left(\frac{P_{yield}^*}{\gamma/L^*} \right) = 2. \quad (6.4)$$

These are the rigid-channel and the infinitely-flexible-channel results, respectively.

Equation (6.3a) shows that increasing wall flexibility decreases $P_{yield}^*/(\gamma/H)$ by increasing the upstream channel width. However, the limits given by (6.4) show that wall flexibility can decrease the meniscus radius of curvature to half of the upstream channel half-width, which doubles the P_{yield}^* that would be expected based solely upon a rigid-channel analysis using the upstream channel width, the approach originally taken by Macklem (1971). This result most closely matches the measurements by Perun & Gaver (1995a) ($P_{yield}^* \sim 1.85\gamma/L^*$). However, the prediction greatly underestimates the 'apparent' P_{yield}^* from Perun & Gaver (1995b), and tube experiments by Gaver *et al.* (1990) and Hsu *et al.* (1994). The discrepancies between tube measurements and channel predictions are likely to be due to differences in the meniscus curvature associated with the three-dimensional buckling of the tube near the meniscus tip. This rationale is not sufficient to explain the large discrepancy with the measurements by Perun & Gaver (1995b). Instead, as will be discussed below in §6.3, this variance may be attributable to stability behaviour.

6.3. Stability

The multiple branch behaviour of the P_b vs. Ca relationship suggests the possibility of instability of one, or both, of the branches of the response curve. The analysis presented in this paper does not use a time-dependent approach that could be used to investigate the stability of each of the branches. However, it is useful to consider the data in relation to experiments conducted in flexible-walled systems to develop an idea of the stability behaviour that one might expect.

In experimental investigations, either P_b^* or the flowrate of air (Q^*) are set, and the corresponding $P_b^* - U$ relationships are measured. Theoretically, U is multi-valued for a given P_b^* , so pressure-driven experiments and time-dependent simulations with fixed P_b^* might show unsteady behaviour near unstable branches that could include the migration from an unstable steady branch to the stable branch. Flow-rate-driven experiments cannot show this behaviour, since P_b^* is a single-valued function of Q^* . Nevertheless, stability characteristics can be ascertained from those types of experiments. Recent experiments by Gaver *et al.* (1990), Perun & Gaver (1995a, b) and Hsu *et al.* (1994) employed flowrate-driven systems.

Of these experiments, those of Perun & Gaver (1995b) most closely resemble conditions posed by the theory described herein. In particular, these experiments evaluated the steady-state response of a bubble constrained within a channel with one rigid, and one nearly linearly-elastic wall. Although it is beyond the scope of the present paper to provide a detailed comparison between the experimental and theoretical results, the experiments did show characteristics predicted by the theory. For example, the experiments showed an increase in P_b with increasing Γ and η . However, these studies did not demonstrate left-hand-branch behaviour with $\Gamma = 0.01$ over the range $0.1 < Ca < 8$ and $\Gamma = 0.6$ over $0.8 < Ca < 10$, where $\Gamma_{exp} = K_{exp} H^2/\gamma$ was based on the elasticity (K_{exp}) of the compliant channel wall. Unfortunately, the minimum Ca for these experiments is greater than the transitional Ca predicted by the theory (strict comparison between the Γ_{exp} and Γ_{theory} must be made with caution). Smaller values of Ca were not reported owing to a lack of steadiness of P_b . So, this evidence suggests that the left branch of the $P_b - Ca$ relationship may be unstable. In addition, according to the results of §6.2, steady-state meniscus motion cannot exist when $P_{yield}^* < P_b^* < P_{min}^*$. This provides further evidence for left-hand branch instability.

Other related experiments by Gaver *et al.* (1990), Perun & Gaver (1995a) and Hsu *et al.* (1994) used systems with highly nonlinearly elastic walls. None of these studies

reported data consistent with the left-hand branch of the P_b - Ca relationship. However, Perun & Gaver (1995a) analysed the P_b^* steadiness during their experiments. They found that although the average P_b decreased with decreasing Ca (consistent with the right-hand branch), data from $Ca < 0.5$ was increasingly unsteady. Interestingly, data from the unsteady measurements, when averaged, followed a monotonic trend that was continuous with the large Ca (right-hand branch) steady-state response. For highly compliant systems, this unsteady branch may be very short, since P_{min} occurs at very small Ca . In this case, the resulting ‘apparent’ P_{yield}^* nearly equals the theoretical prediction of P_{yield}^* , as demonstrated by Perun & Gaver (1995a). For less compliant systems, the experiments suggest that low Ca behaviour, when averaged, results in an ‘apparent’ P_{yield}^* that does not correspond to static predictions of the true P_{yield}^* , as demonstrated by Perun & Gaver (1995b). So, the unsteady left-hand branch, if it exists, may not connect to the static prediction of P_{yield}^* unless $\Gamma \ll 1$. This hypothesis is speculative, since the experimental systems do not completely mimic the theoretical model.

6.4. Limitations

As with any model study, this investigation includes simplifications that limit the model validity and the degree with which the model can be compared to true physical systems. The major assumptions of this study relate to simplifications of the wall equation leading to (2.4). We assumed that owing to inextensibility, shear stress would result in variation in T , but would not lead to tangential extension of the wall. However, we further assumed that the shear stress-induced variation of wall tension did not greatly modify the wall tension from the average wall tension in the system. A macroscopic control-volume analysis of the x -component of linear momentum using a control volume surrounding the entire domain shows that this global variation in wall tension is $\Delta T = P_b^* L^* - \gamma$, where ΔT is the tension difference between the far upstream and downstream ends of the domain and L^* is the upstream channel half-width. This variation is negligible if $P_b^2/(\eta\Gamma) \ll 1$. This relationship is satisfied in all simulations within this study with the exception of the $\eta = 2$ calculation in figure 16, which was used only for illustrative purposes related to turnaround behaviour.

Another limitation relates to the model’s ability to mimic true airway geometrical characteristics. Actual airways are roughly circular when inflated, and collapse to a more complicated geometry. In the upstream region, the circular airway has a transverse component of curvature, which is neglected in the two-dimensional model. This curvature component is the source of capillary-elastic instabilities, which can cause meniscus formation if $H/R^* > 0.12$ (Halpern & Grotberg 1992). By analogy, this result suggests that the reopened portion of the airway would remain patent if $H/L^* \sim \Gamma/P_b < 0.12$, suggesting that low Γ (large compliance) may be important for preserving airway patency. Future studies should investigate how this behaviour influences reopening phenomena.

We have also assumed that the collapsed region is planar, and that this dictates the meniscus geometry. By comparing the predictions from the present model to channel (Perun & Gaver 1995a, b) and tube (Gaver *et al.* 1990; Hsu *et al.* 1994) studies, it is evident that the three-dimensional buckling geometry can influence the reopening pressures. This buckling geometry may be much more complicated than the ribbon-like flattened mode investigated in the tube experiments.

Furthermore, we have assumed that the airway walls are massless and are supported by a linearly elastic material. Clearly, these approximations are not completely accurate. From experimental measurements, we may infer that nonlinear wall responses may reduce, or eliminate, the left branch of the P_b - Ca relationship.

Finally, this study ignores the influence of surfactant on the bubble interface. In actual airway reopening, surfactant transport along the bubble interface and between the bulk fluid and the interface could greatly influence the interfacial stresses. This coupled physicochemical system may be of great importance towards understanding pulmonary mechanical behaviour, and will be the subject of future investigations.

6.5. Summary

In this paper, we have developed and analysed an initial model of pulmonary airway reopening. This model includes the interaction between fluid and structural forces as a finger of air is forced through a compliant channel. We have shown that two important regimes of the flow behaviour exist. The first (left-hand branch) occurs when $Ca \ll \min(1, (\Gamma^3/\eta)^{1/2})$, and is governed by the interaction of surface tension and elastic stresses. In this regime, a decrease of P_b increases the reopening velocity. This is due to a shortening of the transition segment connecting the fully inflated airway to the fully collapsed region, decreasing the resistance to flow. Another regime (right-hand branch) occurs when $\max(1, (\Gamma^3/\eta)^{1/2}) \ll Ca \ll \eta$. This regime is governed by the balance between fluid viscous and longitudinal wall tension forces, and results in a monotonically increasing P_b - Ca relationship. Increasing η or decreasing Γ reduces the Ca associated with the transition from one branch to the other.

Start-up yield pressures are predicted to range from $1 \leq P_{yield}^*/(\gamma/L^*) \leq 2$, with highly compliant walls decreasing the meniscus curvature, thus increasing $P_{yield}^*/(\gamma/L^*)$. However, predictions of minimum pressures for steady-state reopening show that $P_{min}^*/(\gamma/L^*) \sim 6\gamma/L^*$ for highly compliant channels ($\Gamma = 0.05$). Since $P_{yield}^* < P_{min}^*$, this suggests that low Ca reopening may be unsteady, a behaviour that has been observed experimentally. Experimentally, this unsteady behaviour, when averaged, appears to continue monotonically from the right-hand branch of the P_b - Ca relationship.

Finally, our predictions are consistent with experimental observations that show the bubble pressure in highly compliant channels scales with γ/L^* , where L^* is the upstream channel width. In contrast, we find that wall shear stresses scale with γ/H . The wall shear and normal stresses occurring during reopening are potentially very large and may be physiologically significant.

D.P.G. appreciates the many helpful discussions with Drs J. Solway and R. W. Samsel related to the development of this study. This research was funded by NSF grants BCS-9358207, BCS-9209558 and CTS-9013083, NIH grant HL51334, NASA grant NIG-31636, NATO grant CRG-950725 and the Whitaker Foundation.

Appendix A

In this Appendix we derive the linear lubrication approximations that are used for boundary conditions for regions I and II.

Region I

Conditions at the upstream end of region I, $x \rightarrow -\infty$, which are needed to solve (3.6), are obtained by linearizing equations about $h = L$ and $f = L - 1$. To do so, we obtain a uniform perturbation expansion by letting

$$\left. \begin{aligned} h &= L + \epsilon h_1 + \epsilon^2 h_2, \\ f &= L - 1 + \epsilon f_1 + \epsilon^2 f_2, \end{aligned} \right\} \quad (\text{A } 1)$$

where $\epsilon \ll 1$ represents the magnitude of the deviation from the uniform upstream conditions. At $O(\epsilon)$ we get the following system:

$$\left. \begin{aligned} \Gamma h_1' - \eta h_1''' &= -3Ca(h_1 - f_1), \\ f_1' + \eta h_1'' &= \Gamma h_1. \end{aligned} \right\} \quad (\text{A } 2)$$

The solutions for h_1 and f_1 are exponentials of the form e^{mx} where m satisfies a quintic polynomial,

$$\eta m^5 - \Gamma m^3 - 3Ca(\eta + 1)m^2 + 3Ca\Gamma = 0. \quad (\text{A } 3)$$

It can be shown that for any η , Γ and Ca , the above polynomial has two positive real roots m_1 and m_2 , provided $\eta \neq 0$. If $\eta = 0$ then there is only one positive real root. Hence the functions h_1 and f_1 that decay as $x \rightarrow -\infty$ are given by

$$\left. \begin{aligned} h_1 &= A e^{m_1 x} + B e^{m_2 x} = e_1 + e_2, \\ f_1 &= \left(\frac{\Gamma}{m_1^2} - \eta \right) e_1 + \left(\frac{\Gamma}{m_2^2} - \eta \right) e_2, \end{aligned} \right\} \quad (\text{A } 4)$$

where A and B are free parameters that are varied until the desired shapes are obtained at the downstream end. At $O(\epsilon^2)$, we get the following system for h_2 and f_2 :

$$\left. \begin{aligned} \Gamma h_2' - \eta h_2''' &= 9Ca(h_1 - f_1)^2 - 3Ca(h_2 - f_2), \\ f_2' + \eta h_2'' &= \Gamma h_2. \end{aligned} \right\} \quad (\text{A } 5)$$

In this case only the particular solutions need to be determined:

$$\left. \begin{aligned} h_2 &= b_1 e_1^2 + b_2 e_2^2 + b_3 e_1 e_2, \\ f_2 &= c_1 e_1^2 + c_2 e_2^2 + c_3 e_1 e_2, \end{aligned} \right\} \quad (\text{A } 6)$$

where

$$\left. \begin{aligned} b_j &= -9Ca \alpha_j \frac{K_j^2}{(\eta K_j^5 - \Gamma K_j^3 - 3Ca(\eta + 1)K_j^2 + 3Ca\Gamma)}, \\ c_j &= \left(\frac{\Gamma}{K_j^2} - \eta \right) b_j, \end{aligned} \right\} \quad (\text{A } 7)$$

for $j = 1, 2, 3$, and where $K_j = 2m_j$ for $j = 1, 2$, $K_3 = m_1 + m_2$, $\alpha_j = L_j^2$ for $j = 1, 2$, $\alpha_3 = 2L_1 L_2$ and $L_j = 1 + \eta - \Gamma/(m_j^2)$.

Region II

The boundary condition as $x \rightarrow \infty$ for (3.7) is obtained by linearizing about $h = 1$, using the regular perturbation expansion $h = 1 + \epsilon h_1 + O(\epsilon^2)$. At $O(\epsilon)$, this expansion gives $\eta h_1''' - \Gamma h_1' - 3Ca h_1 = 0$. The possible solutions are given by

$$h_1 = C e^{m_3 x} + D e^{m_4 x} \quad \text{if} \quad \frac{Ca^2 \eta}{\Gamma^3} < \frac{4}{243}, \quad (\text{A } 8a)$$

$$h_1 = (C + Dx) e^{m_3 x} \quad \text{if} \quad \frac{Ca^2 \eta}{\Gamma^3} = \frac{4}{243}, \quad (\text{A } 8b)$$

$$h_1 = e^{m_3 x} (C \sin m_4 x + D \cos m_4 x) \quad \text{if} \quad \frac{Ca^2 \eta}{\Gamma^3} > \frac{4}{243}, \quad (\text{A } 8c)$$

where $m_3 < 0$, $m_4 < 0$ in (A 8a), $m_3 < 0$ in (A 8b) and $m_3 \pm i m_4$ with $m_3 < 0$ in (A 8c) are the roots of the characteristics equation $\eta m^3 - \Gamma m - 3Ca = 0$.

	<i>AB</i>	<i>BC</i>	<i>CD</i>	<i>DE</i>	<i>EA</i>
Location	$x = x_{right}, y = y_w$	$x = x_{right}, y = 0$	$x = 0, y = 0$	$x = x_{left}, y = y_m$	$x = x_{left}, y = y_w$
Boundary conditions	$\tau_{x,A}$ v	u $\tau_{y,B}$	$\tau_{x,C}$ v	$\tau_{x,D}$ $\tau_{y,D}$	$\tau_{x,E}$ $\tau_{y,E}$

	u $\tau_{y,B}$	$\tau_{x,C}$ v	$\tau_{x,D}$ $\tau_{y,D}$	$\tau_{x,E}$ $\tau_{y,E}$	$\tau_{x,A}$ v

TABLE 1. Boundary conditions applied to corner nodes of the computational domain. Entries above the dashed line represent conditions applied on the element preceding the corner node (in the counterclockwise direction), and entries beneath the dashed line represent conditions that following the corner node. Subscripts represent the stress component and the associated element.

Appendix B

This Appendix describes implementation considerations that were significant for evaluating the boundary-element computations of this problem.

Owing to discontinuities in the normal directions at the juncture between corner elements, it is necessary to impose stress discontinuities at the corner points as described in (Halpern & Gaver 1994). This stress-vector discontinuity is due only to a discontinuity in the normal vector at the corner, and has no other physical significance. In our computations, we use a corner-point conditions that specify at least one stress on each of the element nodes that connect to the corner, as described in table 1.

As described by (2.3), stress jumps across the air-liquid interface and elastic walls are related to the domain curvature, $\kappa_{int} = \nabla_s \cdot \mathbf{n}$. The curvature was computed at each interface and wall node *I* by

$$(\kappa_{int})_i = (x_{ss})_i (y_s)_i - (x_s)_i (y_{ss})_i, \quad (\text{B } 1)$$

where the subscript *s* denotes differentiation with respect to the arclength *s*. The arclength to each node (s_i) was computed by integration x_i vs. y_i using a quadratic spline approximation to the interface shape. Cubic splines along the air-liquid interface were computed for x_i vs. s_i and y_i vs. s_i , with specified derivative conditions at the meniscus tip to ensure interfacial symmetry. We used a non-uniform distribution of points along the air-liquid interface to concentrate interface points near the meniscus tip, since the curvature changes rapidly near this location. The point distribution was

$$s_i = s_{total} \frac{\sum_{j=2}^{j=i} (j-1)^{0.5}}{\sum_{j=2}^{j=N} (j-1)^{0.5}}, \quad (\text{B } 2)$$

where $i = 1$ designates the location of the air-liquid interface tip, $i = N$ specifies the last point on the interface, and s_{total} is the total meniscus arclength. Wall points were distributed uniformly.

When coupling solutions using the boundary-element method, we found it convenient to rescale the boundary-value problem using the scales

$$\mathbf{x}^* = L^* \mathbf{x}, \quad \mathbf{u}^* = U \mathbf{u}, \quad P^* = P_b^* P. \quad (\text{B } 3)$$

Here, the lengthscale, $L^* = (P_b^*/K + H)$, represents the upstream channel half-width, and is chosen for several reasons. First, the lengthscale is likely to be related to the meniscus tip radius of curvature, as suggested by our previous experimental studies

(Gaver *et al.* 1990), and thus is useful in representing the meniscus tip pressure drop. Also, by scaling y^* with L^* , the scaled domain is in the range $-1 \leq y \leq 1$, which is independent of P_b . Practically, this scale is useful in studying different bubble pressures, since rough similarity between the scaled domains for different values of P_b exists. This facilitates the transition between domains when transitioning from one parameter range to another. Finally, by scaling x^* with L^* , the domain length increases with P_b . This helps to assure that lubrication approximations are valid at the ends of the boundary-element domain.

REFERENCES

- BREBBIA, C. A. & DOMINGUEZ, J. 1989 *Boundary Elements – An Introductory Course*. Computational Mechanics, Southampton, UK.
- BRETHERTON, F. P. 1961 The motion of long bubbles in tubes. *J. Fluid Mech.* **10**, 166–188.
- COYLE, D. J., MACOSKO, C. W. & SCRIVEN, L. E. 1986 Film-splitting flows in forward roll coating. *J. Fluid Mech.* **171**, 183–207.
- GAVER, D. P., SAMSEL, R. W. & SOLWAY, J. 1990 The effects of surface tension and viscosity on airway opening. *J. Appl. Physiol.* **69**(1), 74–85.
- GREAVES, I. A., HILDEBRANDT, J. & HOPPIN, F. G. 1986 Micromechanics of the lung. In: *Handbook of Physiology: The Respiratory System, Mechanics of Breathing*, sect. 3, vol. 3, pt. 1, chap. 14, pp. 195–216, Am. Physiol. Soc., Bethesda, MD, USA.
- GROTBORG, J. B. 1994 Pulmonary and transport phenomena. *Ann. Rev. Fluid Mech.* **26**, 529–571.
- HALPERN, D. & GAVER, D. P. 1994 Boundary element analysis of the time-dependent motion of a semi-infinite bubble in a channel. *J. Comput. Phys.* **115**(2), 366–375.
- HALPERN, D. & GROTBORG, J. B. 1992 Fluid-elastic instabilities of liquid-lined flexible tubes. *J. Fluid Mech.* **244**, 615–632.
- HALPERN, D. & GROTBORG, J. B. 1993 Surfactant effects on fluid-elastic instabilities of liquid-lined flexible tubes – a model of airway closure. *J. Biomech. Engng* **115**(3), 271–277.
- HALPERN, D. & SECOMB, T. W. 1989 The squeezing of red blood cells through capillaries with near-minimal diameters. *J. Fluid Mech.* **203**, 381–400.
- HALPERN, D. & SECOMB, T. W. 1991 Viscous motion of disk-shaped particles through parallel-sided channels with near-minimal widths. *J. Fluid Mech.* **231**, 545–560.
- HSU, S., STROHL, K. P. & JAMIESON, A. 1994 Role of viscoelasticity in the tube model of airway reopening. I. Nonnewtonian sols. *J. Appl. Physiol.* **76**, 2481–2489.
- JOHNSON, M., KAMM, R. D., HO, L. W., SHAPIRO, A. & PEDLEY, T. J. 1991 The nonlinear growth of surface-tension-driven instabilities of a thin annular film. *J. Fluid Mech.* **233**, 141–156.
- KAMM, R. D. & SCHROTER, R. C. 1989 Is airway closure caused by liquid film instability? *Respir. Physiol.* **75**, 141–156.
- LADYZHENSKAYA, O. A. 1963 *The Mathematical Theory of Viscous Incompressible Flow*. Gordon and Breach.
- LANDAU, L. & LEVICH, B. 1942 Dragging of a liquid by a moving plate. *Acta Phys-chim. URSS* **17**, (1–2), 42–54.
- MC EWAN, A. D. & TAYLOR, G. I. 1966 The peeling of a flexible strip attached by a viscous adhesive. *J. Fluid Mech.* **26**, 1–15.
- MACKLEM, P. T. 1971 Airway obstruction and collateral ventilation. *Physiol. Rev.* **51**, 368–436.
- MACKLEM, P. T., PROCTOR, D. F. & HOGG, J. C. 1970 The stability of peripheral airways. *Respir. Physiol.* **8**, 191–210.
- NAURECKAS, E. T., DAWSON, C. A., GERBER, B. S., GAVER, D. P., GERBER, H. L., LINEHAN, J. H., SOLWAY, J. & SAMSEL, R. 1994 Airway reopening pressure in isolated rat lungs. *J. Appl. Physiol.* **76**(3), 1372–1377.
- OTIS, D. R., JOHNSON, M., PEDLEY, T. J. & KAMM, R. D. 1993 The role of pulmonary surfactant in airway closure – a computational study. *J. Appl. Physiol.* **75**(3), 1323–1333.
- PARK, C. W. & HOMS, G. M. 1984 Two-phase displacement in Hele-Shaw cell: theory. *J. Fluid Mech.* **139**, 291–308.

- PERUN, M. L. & GAVER, D. P. 1995*a* An experimental model investigation of the opening of a collapsed untethered pulmonary airway. *J. Biomech. Engng* **117**, 245–253.
- PERUN, M. L. & GAVER, D. P. 1995*b* The interaction between airway lining fluid forces and parenchymal tethering during pulmonary airway reopening. *J. Applied Physiol.* **75**, 1717–1728.
- RATULOWSKI, J. & CHANG, H. C. 1990 Marangoni effects of trace impurities on the motion of long gas bubbles in capillaries. *J. Fluid Mech.* **210**, 303–328.
- REINELT, D. A. & SAFFMAN, P. G. 1985 The penetration of a finger into a viscous fluid in a channel and tube. *SIAM J. Sci. Stat. Comput.* **6**, 542–561.
- SAFFMAN, P. G. & TAYLOR, G. I. 1958 The penetration of a fluid into a porous medium or Hele-Shaw cell containing a more viscous liquid. *Proc. R. Soc. Lond. A* **245**, 312–329.
- WISWELL, T. E. & MENDIOLA, J. 1993 Respiratory distress syndrome in the newborn: innovative therapies. *Am. Fam. Phys.* **47**, 407–414.
- YAP, D. Y. K., LIEBKEMANN, W. D., SOLWAY, J. & GAVER, D. P. 1994 The influence of parenchymal tethering on the reopening of closed pulmonary airways. *J. Appl. Physiol.* **76**(5), 2095–2105.